

# Transfer report

Literature Review

**Mitchell Watts**



Department of Physics

UCL

January 2017

# Contents

<b>1</b>	<b>Introduction</b>	<b>5</b>
1.1	2D Materials - General Ideas . . . . .	5
<b>2</b>	<b>Literature Review - Black Phosphorus, Bulk and Few-Layer</b>	<b>7</b>
2.1	Structure . . . . .	7
2.1.1	Bulk Black Phosphorus . . . . .	7
2.1.2	Phosphorene . . . . .	7
2.1.3	Diffraction . . . . .	8
2.2	Electronic and optical . . . . .	11
2.2.1	Band structure . . . . .	11
2.2.2	Transport . . . . .	12
2.2.3	Optical . . . . .	12
2.2.3.1	Extinction coefficients . . . . .	13
2.2.3.2	Optical Microscopy . . . . .	13
2.3	Phononic . . . . .	13
2.3.1	Black Phosphorus (Bulk) . . . . .	13
2.3.2	Phosphorene . . . . .	15
2.3.3	Thermal . . . . .	15
2.4	Physical and air stability . . . . .	15
2.4.1	Dominant oxidation reaction . . . . .	16
2.4.2	Secondary oxidation mechanism . . . . .	18
2.5	Synthesis and Modification . . . . .	19
2.5.1	Black Phosphorus . . . . .	19
2.5.2	Phosphorene . . . . .	19
2.5.2.1	Mechanical . . . . .	19
2.5.2.2	Liquid-Phase . . . . .	19
2.5.2.3	Growth . . . . .	20
2.5.2.4	Etching . . . . .	20
2.5.2.5	Modification . . . . .	20
2.6	Applications . . . . .	26
2.7	Phosphorene Nanoribbons . . . . .	26
2.7.1	Isolation . . . . .	26
2.7.2	Properties . . . . .	27
2.7.2.1	Electronic and optical . . . . .	27
2.7.2.2	Phononic and thermal . . . . .	29
2.7.3	Applications . . . . .	30

<b>3 Literature Review - Techniques</b>	<b>32</b>
3.1 Diffraction . . . . .	32
3.2 TEM . . . . .	33
3.2.1 Components of a TEM . . . . .	33
3.2.1.1 Gun and monochromator . . . . .	34
3.2.1.2 The specimen . . . . .	34
3.2.1.3 Condenser lenses . . . . .	34
3.2.1.4 Objective aperture . . . . .	34
3.2.1.5 STEM . . . . .	35
3.2.2 Resolution . . . . .	35
3.2.3 Contrast . . . . .	36
3.2.4 Analysis . . . . .	36
3.2.5 Other notes . . . . .	37
3.3 AFM . . . . .	37
3.3.1 Types . . . . .	37
3.3.1.1 Contact . . . . .	38
3.3.1.2 Tapping . . . . .	38
3.3.1.3 Non-contact mode . . . . .	39
3.3.1.4 High speed AFM . . . . .	39
3.3.2 Artefacts . . . . .	39
3.3.2.1 Scanner/piezo . . . . .	39
3.3.2.2 Tip . . . . .	39
3.3.2.3 Feedback . . . . .	39
3.4 XPS . . . . .	40
<b>4 Methodology</b>	<b>41</b>
4.1 Metal-Ammonia solutions . . . . .	41
4.1.1 Decomposition . . . . .	41
4.2 Dissolution/suspension . . . . .	42
4.2.1 Overview of DLVO . . . . .	42
4.2.2 Spontaneous dissolution . . . . .	43
4.2.3 Suspensions vs solutions . . . . .	44
<b>5 Research question</b>	<b>45</b>
<b>6 Work so far</b>	<b>46</b>
6.1 Nanoribbons . . . . .	46
6.1.1 Evidence of intercalation . . . . .	46
6.1.1.1 Visual evidence . . . . .	46
6.1.1.2 Xray diffraction of intercalant . . . . .	47
6.1.1.3 In-situ neutron diffraction . . . . .	50
6.1.1.4 Xray photoelectron spectroscopy . . . . .	50
6.1.2 Evidence of exfoliation . . . . .	52
6.1.2.1 TEM of exfoliated product . . . . .	52
6.1.2.2 AFM of exfoliated product . . . . .	53
6.1.3 Evidence of mechanism . . . . .	55
6.1.4 Controls . . . . .	56
6.2 Planned experiments . . . . .	58
6.3 Other work . . . . .	59

6.3.1	Sodium-ion battery anode . . . . .	59
6.3.2	Ogg glasses . . . . .	59
6.3.3	Additonal beamtime . . . . .	60

<b>7</b>	<b>Plan and timetable</b>	<b>61</b>
----------	---------------------------	-----------

# Chapter 1

## Introduction

Low dimensional materials have become an increasingly active research area since the isolation of graphene in 2004 by Novoselov and Geim [1]. Recently, a new layered material has been the subject of research, due to the possibility of exfoliation into its 2D form. This material is black phosphorus (BP), and it will be the subject of this review.

Like graphene, the 2D form of black phosphorus - called phosphorene, is mono-elemental, meaning it is composed entirely of one atomic species. Phosphorene is also interesting due to its novel properties, such as a bandgap which is highly tuneable by layer number, sheet width, external stresses and electric fields. Additionally, it possesses intermediate values of band gap and mobility compared to graphene or TMDCs, for this reason researchers often refer to BP as 'bridging the gap' between graphene and TMDCs.

In this report the characterisation methods which are used for identifying few layer black phosphorus are discussed, as well as research on black phosphorus, its properties, success in the field and possible applications of it - including its nanoribbon counterpart. The future of the project is also discussed.

### 1.1 2D Materials - General Ideas

A two-dimensional (2D) material is one which is confined in one dimension, resulting in a 'sheet' of material. This can be one, or multiple atoms thick, and may be flat or puckered. Examples of 2D materials include graphene,  $MoS_2$  and recently, phosphorene. These can be exfoliated from the bulk or grown, depending on the material, for example silicene can only be grown on a substrate (as can blue phosphorene for now). 1D materials have further confinement in another direction, examples include graphene nanoribbons and carbon nanotubes. Further dimensional confinement can result in 0D materials, or quantum dots.

Low-dimensional materials are interesting due to band gap modifications or the effects of quantum confinement. Quantum confinement occurs when a dimension of the material approaches the exciton Bohr radius of the bulk material. The exciton Bohr radius is the distance between an electron-hole pair. This problem becomes similar to a particle in a box situation, changing the continuous band-like distribu-

tion of allowed states into discrete energy levels, reminiscent of those found in atoms (if the dimensions are extended in one or more dimensions then the overall band structure is intact but modified). To model this particle in a box the hole typically has a negative electron mass with positive charge and the system is modelled like the hydrogen atom with the reduced mass of the system as the mass. The exciton Bohr radius can be defined as:

$$a_b^* = \epsilon_r \left( \frac{m}{\mu} \right) a_b \quad (1.1.1)$$

Where  $\mu$  is the exciton reduced effective mass,  $a_b$  is the Bohr radius=0.053nm (most probable distance between proton and electron in H atom), and  $\epsilon_r$  is size dependent dielectric constant.

Further quantum confinement in black phosphorus below a 2D material is interesting due to anisotropic carrier masses in the in-plane lattice directions. This means that different confinement effects will be observed for 1D black phosphorus depending on the orientation

The Schrödinger equation for a 2D quantum well is:

$$E_n(k_x k_y) = \frac{\pi^2 \hbar^2 n^2}{2m^* L_z^2} + \frac{\hbar^2}{2m^*} (k_x^2 + k_y^2), \psi = \phi(z) \exp(ik_x x + k_y y) \quad (1.1.2)$$

The solutions of this depend not only on the thickness of the material, but on the potential of the materials around it. If these are infinitely high then the material is isolated and the energy solutions are simple:

$$E_n = \frac{\pi^2 \hbar^2 n^2}{2m^* L_z^2}, n = 1, 2, \dots \quad (1.1.3)$$

and

$$\phi_n = A \sin\left(\frac{n\pi z}{L_z}\right) \quad (1.1.4)$$

If the material at the boundaries is not a vacuum, then there will be some tunnelling of electrons and these solutions will change accordingly.

# Chapter 2

## Literature Review - Black Phosphorus, Bulk and Few-Layer

Since the isolation of the 2D counterpart, renewed interest has been found in BP, with a range of potential applications. Additionally, researchers have undertaken in-depth characterisation, in order to better understand the 2D form. The bulk of research, however, has focused on the FL form of BP. This is due primarily to interesting effects when reducing dimensionality in the stacking axis. Here we describe the physical, electronic and optical, and phononic properties as well as issues with stability.

### 2.1 Structure

#### 2.1.1 Bulk Black Phosphorus

Black phosphorus (BP) is a layered material, similar in many ways to graphite in terms of structure, the most noticeable difference being that each layer is puckered. Black phosphorus is strongly bonded in plane, with weak out of plane bonds, which allows the exfoliation of 2D layers, which will be discussed in detail later.

Each phosphorus atom has 5 valence electrons, unlike the four present in graphite. This gives a shell configuration of  $3s^23p^3$ , and each phosphorus atom bonds to three neighbouring atoms. This produces  $sp^3$  hybridisation, similar to that seen in ammonia, leading to a puckered honeycomb lattice as seen in figures 2.1 and 2.2 [2,3]. The anisotropic structure found in BP leads to unusual mechanical, electronic and optical effects, which will be investigated below.

BP is typically studied in its orthorhombic structure, although at high pressure it can also adopt a hexagonal structure (arsenic A7) which has been called 'blue phosphorus'- another allotrope of phosphorus with a direct bandgap of 2eV [2]. It can also adopt a simple cubic structure at very high pressures above 8GPa [5].

#### 2.1.2 Phosphorene

When the layer number of BP decreases towards a 2D material, the lattice constants along the armchair (AC) direction increase and along the zigzag (ZZ) direction de-

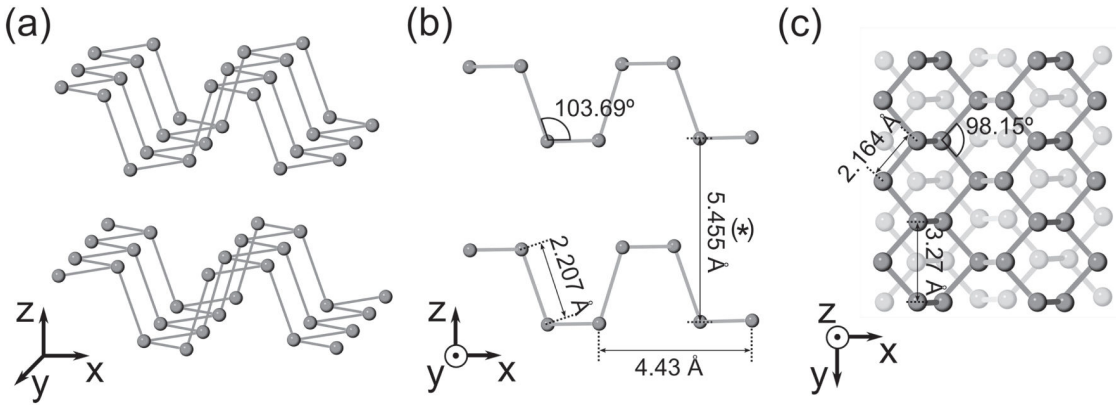


*Figure 2.1: The structure of black phosphorus - note the ABA stacking order of layers. (a) 3D representation. (b) Lateral view. (c) Top view. These structures have been obtained by relaxing structures using DFT calculations. [4]*

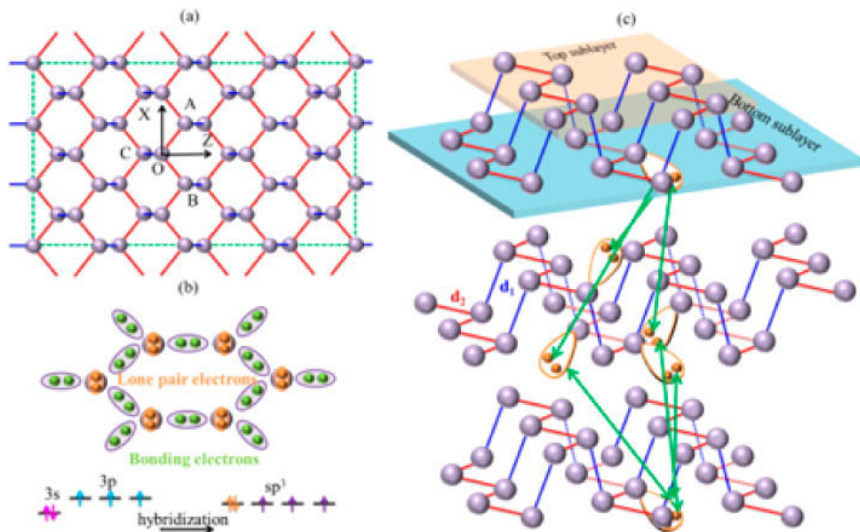


*Figure 2.2: Schematics of (a) the structure of phosphorene, (b) the bonding structure and  $sp^3$  hybridization process, and (c) the mechanism of van der Waals force formation between adjacent layers. The small yellow and green balls represent the lone pairs and bonding electrons, respectively. The separation distance between neighboring layers is approximately 5.0 - 5.5 Å [3]*

crease. This is derived from an increase in bond angle seen through DFT calculations [7, 8]. This change in structure, and hence in electronic and optical structure contributes to interesting changes in properties observed for few layer BP, and has sparked much interest in the research community.

### 2.1.3 Diffraction

X-ray diffraction (XRD) experiments of synthesised BP at 1.2GPa and 1100K (using the bismuth flux method) have been performed [9], Rietveld refinement of the data lead to the lattice parameters and unit cell that is frequently used in BP literature today. There is no evidence to suggest that different methods of production lead to changes in structure.

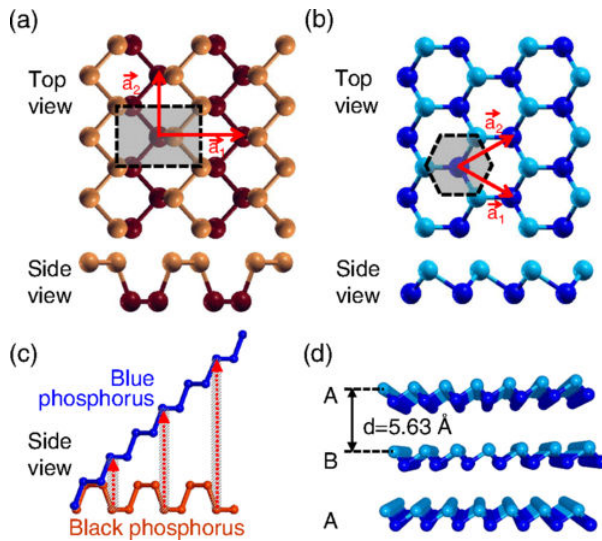


Figure 2.3: The layered structure of (a) black and (b) blue phosphorus in top and side views. Atoms at the top and bottom of the nonplanar layers are distinguished by color and shading, and the Wigner-Seitz cells are shown by the shaded region. (c) Schematic of the conversion of black to blue phosphorus by dislocations, highlighted by the shaded regions and arrows. (d) Equilibrium structure of AB stacked blue phosphorus in side view. [6]

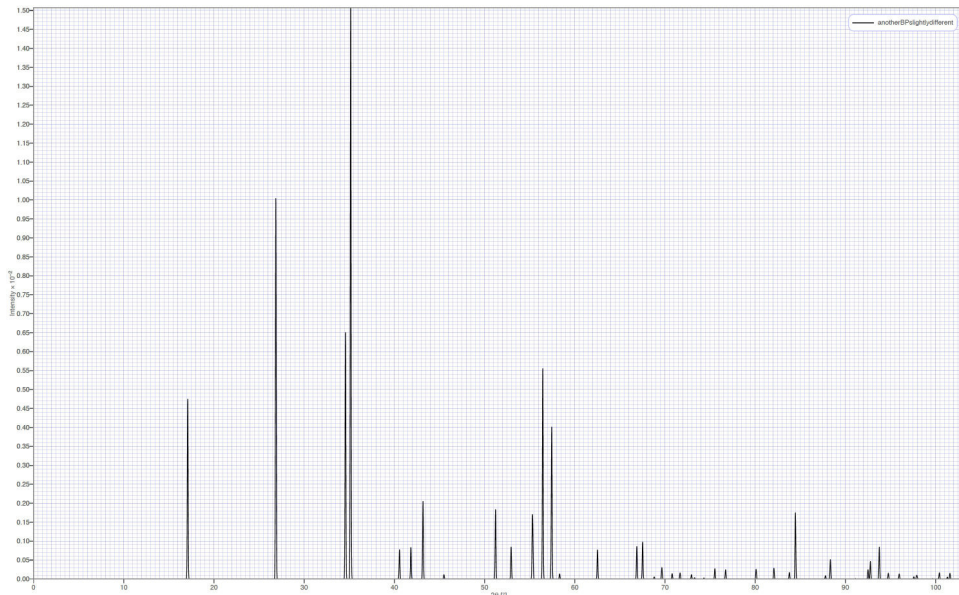
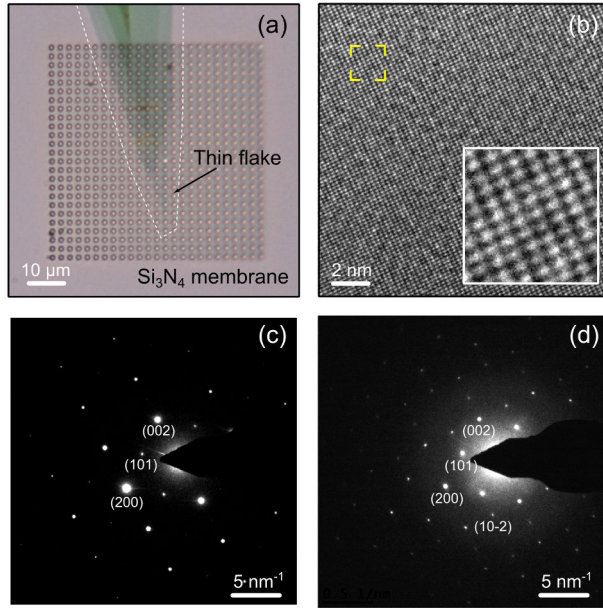


Figure 2.4: XRD simulated powder diffraction pattern from cif file via Reitveld refined experimental powder diffraction of BP [9]

Due to the relatively weak forces between layers, we expect that exfoliated sheets will be in the ac plane, we therefore expect the zone axis in TEM diffraction to be along the b (stacking) axis. This leads to ease of identification when using HRTEM (when viewing atoms) or when performing electron diffraction as seen in figure 2.5 [10–12]. A report by Castellanos-Gomez [4] presents simulated data which can be used to characterise thickness. The 101 reflections are usually forbidden, however due to the strong interaction of electrons with matter, multiple reflections occur on each layer of BP. This means that for odd numbers of layers these reflections are not cancelled out and the 101 peaks can be seen (note a very tiny intensity may be seen for even numbers of layers). The details of these intensity ratios to characterise thickness are shown in table 2.1.

Some researchers utilise mass contrast using STEM to estimate the thickness, however this often relies on calibration with other techniques. Woomer et al. [13]



*Figure 2.5: Transmission electron microscopy study of few-layer black phosphorus flakes. (a) Optical image of a black phosphorus flake transferred onto a holey silicon nitride membrane. (b) High resolution transmission electron microscopy image of the multilayered region of the flake ( $\approx 13\text{-}21$  layers). (c) and (d) are electron diffraction patterns acquired with a 400  $\mu\text{m}$  spot on the thick ( $\approx 13\text{-}21$  layers) and the thin ( $\approx 2$  layers) region of the flake. [4]*

Number of layers	$\frac{I(101)}{I(200)}$
1	2.557
2	0.001
3	0.286
4	0.001
5	0.104
6	0.001
21	0.009

*Table 2.1: The thickness dependence of the intensity ratio between the 101 and 200 reflections. [4]*

also use the difference in counts through TEM, taking account for many factors such as exposure time, aperture selection, lens currents, magnification, and defocus value to study the change in count rate. From this they deduce the thickness, much like in optical transmission characterisation discussed below.

## 2.2 Electronic and optical

### 2.2.1 Band structure

The band structure of BP is shown in figure 2.6 [10, 14]. BP possesses a direct band gap at the  $\Gamma$  point of the Brillouin zone, the size of the band gap can be tuned by altering the number of layers, between 0.3eV and 2eV (with an optical binding energy of about 0.8eV for monolayer BP). The 1-5 $\mu\text{m}$  wavelength range is useful for

applications in the near infrared (NIR), BP has a good optical conductivity in this range, which could lead to applications in thermal imaging, night vision and optical communications [2, 15].

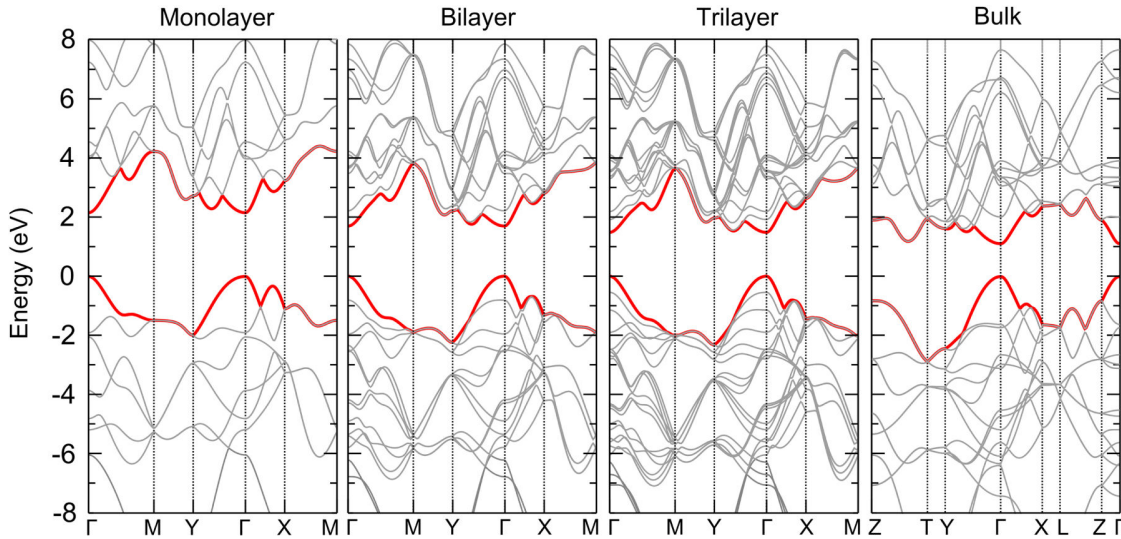


*Figure 2.6: Calculated electronic band structure for monolayer, bilayer, trilayer and bulk black phosphorus sheets at all high-symmetry points in the Brillouin zone. The energy is scaled with respect to the Fermi energy  $E_F$ . [4]*

BP has 16 bands, split into two sets [7]. The lowest two pairs, three pairs below the gap, and three above can be regarded as the 3s, 3p and sp anti-bonding bands respectively. A large direct gap opens at the  $\Gamma$  point between the 3p bonding and anti-bonding bands. The dispersion of the valence band around the  $\Gamma$  point is anisotropic, which leads to the discrepancy in hole mass along the AC and ZZ directions, with a lighter effective mass and therefore greater conductivity along the AC direction.

The bonding-like feature of the valence band is in the interlayer region, so the overlapping of wavefunctions in this region is the origin of the interlayer interaction [7], it is also shown elsewhere that the van der Waals interaction is mostly Keesom forces from out of plane dipole interactions [16] (see figure 2.2). This introduces a band dispersion along Z, which explains the change in band gap with decreasing layers.

The band gap also shifts with decreasing width due to quantum confinement [17–22]. Therefore nanoribbons have been predicted to have interesting properties and will be discussed further below.

## 2.2.2 Transport

BP has been shown to have high hole mobilities in the range of  $100\text{--}1000\text{cm}^2\text{V}^{-1}\text{s}^{-1}$  [11, 23–28], and has been predicted to be as high as  $10000\text{cm}^2\text{V}^{-1}\text{s}^{-1}$  [29], or even higher at low temperatures [25]. This, combined with the large interlayer spacing ( $3.08\text{\AA}$  vs sodium ion size of  $2.04\text{\AA}$ ) has attracted interest from battery engineers as

a possible anode for sodium-ion batteries [30–39].

In addition the on/off ratios for BP have been shown to be in the range of 100-10000, attracting interest from the FET community [18, 24, 40, 41]. There has also been interest from the photovoltaic (PV) community due to the ambipolar field effect in BP [2, 10, 28, 42, 43].

### 2.2.3 Optical

Linear di-chroism is seen in the optical spectra along the Z axis in BP, when polarized along the X or Y directions [44]. The first absorption peak has a strong layer dependence, if polarized along X the first peak is 1.55eV for monolayer BP - decreasing with layer number to 0.46eV in the bulk. For Y polarized light this is 3.14eV in the monolayer and 2.76eV in the bulk.

#### 2.2.3.1 Extinction coefficients

Coleman et al. [45] use extinction coefficients to estimate the concentration of few layer BP in their solutions. The extinction coefficient is defined as:

$$T = 10^{-\epsilon Cl} \quad (2.2.1)$$

Where l is the cell length, C is the nanosheet concentration, T is the optical transmittance and  $\epsilon$  is the extinction coefficient. This includes contributions from the absorbance and the scattering. The scattering is size dependent, therefore the extinction coefficient does not give an accurate estimate of nanosheet concentration. The absorbance coefficient can however be used for concentrations of material in solution.

#### 2.2.3.2 Optical Microscopy

Transmission mode optical microscopy can be used to identify the thickness of large sheets, usually found via mechanical exfoliation. This relies on the use of multiples of % light transmission, with the common multiple being attributed to the monolayer.

## 2.3 Phononic

### 2.3.1 Black Phosphorus (Bulk)

There are 4 atoms in the unit cell of phosphorene and therefore 12 phonon modes, 3 acoustic and 9 optical as seen in figure 2.7 [7, 46]. The optical modes at the  $\Gamma$  point can be classified as  $B_u^1, B_u^2, B_g^2, 2B_g^3, 2A_g, A_u$  and  $B_g^1$ . Therefore there are 12 phonon modes which are:

$$\Gamma = 2A_g + B_{1g} + B_{2g} + 2B_{3g} + A_{1u} + 2B_{1u} + B_{3u} \quad (2.3.1)$$

The acoustic phonon modes can be classified into: two in-planes modes, the TA and LA, and an out of plane ZA mode [47]. The two in-plane modes have linear dispersion, and the Z mode is parabolic. The acoustic phonon modes are anisotropic

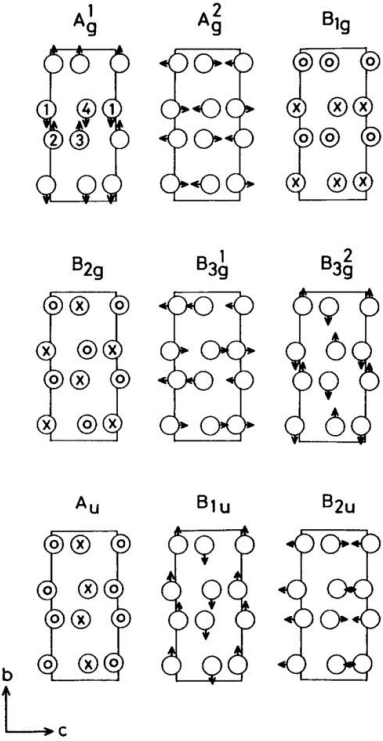


Figure 2.7: Normal modes of the  $\Gamma$ -point optical phonons in black phosphorous. [46]

due to the structure, so the sound velocity of LA in AC direction is different than in ZZ [7]. ZZ has a larger sound velocity, which is where the anisotropy in thermal conductivity arises.

The Raman active modes in BP are  $A_g^1, A_g^2, B_{1g}, B_{2g}, B_{3g}^1, B_{3g}^2$  [48]. Given the usual choice of crystallographic axis, with the incident light along the stacking axis (y axis), the Raman active modes are given by [49]:

$$2A_g + B_{2g} \quad (2.3.2)$$

These are shown in figure 2.8, The peaks are centred at:  $362.1\text{cm}^{-1}$ ,  $439.5\text{cm}^{-1}$  and  $467.7\text{cm}^{-1}$  (and a silicon substrate peak seen at  $520.9\text{cm}^{-1}$ ). These correspond to  $A_g^1, B_{2g}$  and  $A_g^2$  phonon respectively.

Ribeiro [49] and Mao [48] have both investigated the angular dependence of the Raman response in BP. Both have found that the theoretical understanding requires some effects usually not accounted for in other similar materials. Ribeiro claims that by using the imaginary parts of the Raman tensors, the experimental data can be fitted well. The phase differences of the modes which are totally symmetric do not cancel out due to BP's absorption of light. In particular the  $A_g$  modes are poorly fitted without this step. Mao et al. put this difference down to birefringence in the crystal, and also successfully describe the angular response.

### 2.3.2 Phosphorene

The Raman response for phosphorene changes with decreasing number of layers, and a slight shift is seen in the position of the Raman peaks but may not be resolvable. Additionally, the intensity of the modes  $A_g^1$  vs the silicon peak shifts in intensity

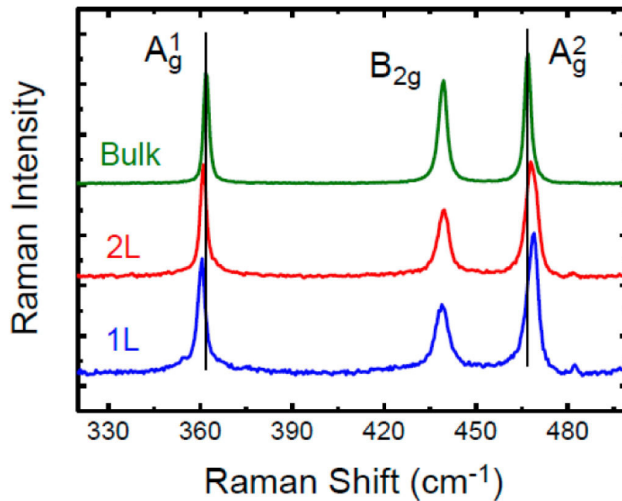


Figure 2.8: Raman spectra of single-layer and bilayer phosphorene and bulk black phosphorus films [25]

linearly up to 15nm thickness, which allows the thickness to be identified, as seen in figure 2.9 [50]. Additionally the  $A_g^1$  and  $A_g^2$  modes also show shifts in their positions, which move together slightly with decreasing thickness, as seen in figure 2.8 [25]. This is because of stiffening of the  $A_g^1$  out of plane mode with decreasing thickness.

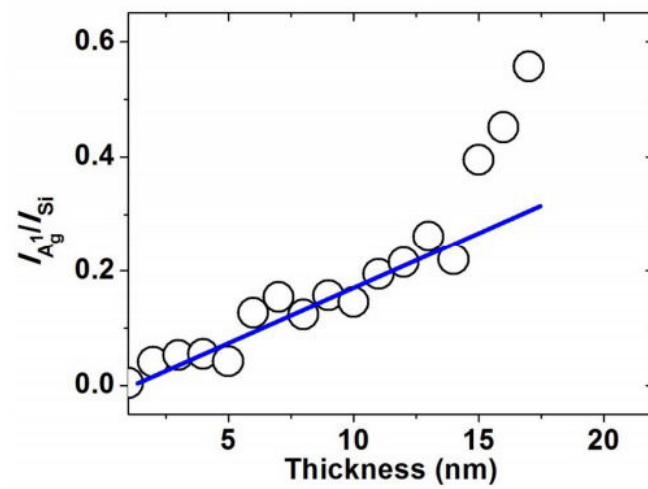


Figure 2.9: Thickness dependence of  $I_{A_g^1}/I_{Si}$  [50]

### 2.3.3 Thermal

A thermoelectric device is one which utilises the Seebeck effect in order to generate electricity. These can be used in power plants, cars and space applications in order to produce electricity from thermal sources. They operate at an atomic level in a similar manner to heat engines, and thus they have a limited efficiency. This efficiency can be characterised by the figure of merit. The figure of merit for thermoelectric devices is given by:

$$ZT = \frac{S^2 \sigma T}{\kappa} \quad (2.3.3)$$

Where S is the Seebeck coefficient,  $\sigma$  is the electrical conductivity and  $\kappa$  is the total thermal conductivity of phonons and electrons. ZT values of greater than one are needed for realistic applications [7]. It has been shown that phosphorene can possess a ZT greater than one in ambient conditions [47, 51]. A ZT value of infinity approaches the Carnot efficiency, so the higher the ZT the better for practical applications.

## 2.4 Physical and air stability

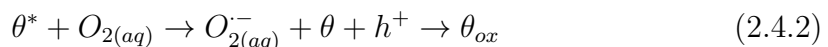
BP is known to be unstable in ambient conditions due to oxidation of the surface, this is attributed to the lone pair on the phosphorus atoms and high valence bond angles of an average 102 degrees [7, 42], as seen in figure 2.1. Many variations on theories for how degradation occurs in BP have been proposed, however there are two main reactions proposed.

### 2.4.1 Dominant oxidation reaction

The first is the dominant reaction occurring in BP, this occurs due to oxidation of the surface, here we discuss the current research on this process.

Many papers have shown that surface roughness of BP increases with time, and that Raman signals which disappear or degrade are linked to this surface roughness [11, 16, 52]. Early work by Castellanos-Gomez suggests that BP has an implicit dipole moment out of plane which makes it hydrophilic, however immersion in DI and de-aerated water does not produce visible droplets, suggesting this is not correct [10, 11, 16, 42, 53]. It appears the surface of BP is in fact only made hydrophilic following oxidation, due to dangling oxygen bonds [53].

The proposed mechanism can be described as:



i.e. optical excitation produces excitons, which then produce charge carriers at surface to transfer towards aqueous oxygen at surface. This then forms a hole in the phosphorene flake, and a super-oxide radical, which immediately oxidises the flake to form oxides [23].

This is derived from Marcus-Gerischer theory, which gives:

$$\frac{d\theta}{dt} = -\theta J_{ph}[O_2] \cdot \exp\left[-\frac{(|E_{g,n})|/2 + E_i - E_{f,redox}^0 - \lambda)^2}{4k_B T \lambda}\right] \quad (2.4.3)$$

where  $J_{ph}$  is the laser flux,  $[O_2]$  is the concentration of oxygen in the surface water,  $E_i$  is the intrinsic Fermi level,  $E_{g,n}$  is the bandgap energy of n layers flake,  $E_{f,redox}^0$  is

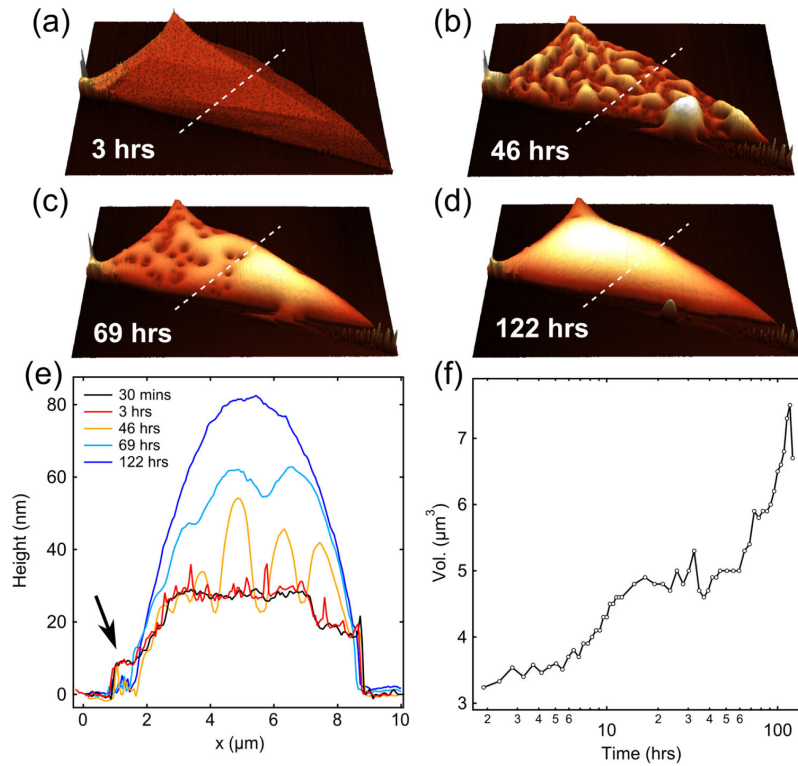
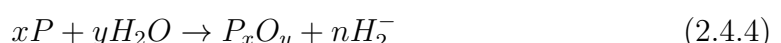


*Figure 2.10: (a)-(d) Selected AFM scans of a BP flake in air taken at (a) 3 hours, (b) 46 hours, (c) 69 hours, and (d) 122 hours after exfoliation. Dotted white lines indicate the position of the line profiles shown in (e). (e) Line profiles taken across the BP flake from the scans in (a)-(d) as well as a line profile for the AFM scan taken directly after exfoliation. (f) Total volume of the flake and water over the measurement period. [16]*

the energy level of the oxygen acceptor states and  $\lambda$  is the re-normalization energy of oxygen in the water. This leads to an exponential dependence on the square of energy gap, see figure 2.12. We therefore expect monolayer BP to oxidise much faster than bulk BP.

Favron suggests that water adsorption forms phosphoric acid which stops oxide accumulation, this is contradictory to other work performed by Huang [11]. The droplets can be removed (cannot be spotted under optical microscopy or AFM) when heated to a temperature of 250C under UHV for 2 hours which suggests they are not just water, but a liquid or dissolved species with a much lower vapour pressure than water such as  $P_xO_y$  species.

A mechanically exfoliated flake suspended in deionized water (non deaerated) causes degradation in 2 weeks, the thinnest parts seem to disappear, suggesting etching [11]. Note that this does not produce roughness on the surface, but a change in optical contrast (hence the etching). This is thought to be because the droplets are formed due to soluble degradation compounds. The lack of droplets on the surface here suggests that pristine BP is not actually hydrophilic. This suggests BP cannot oxidise in water via the following reactions:



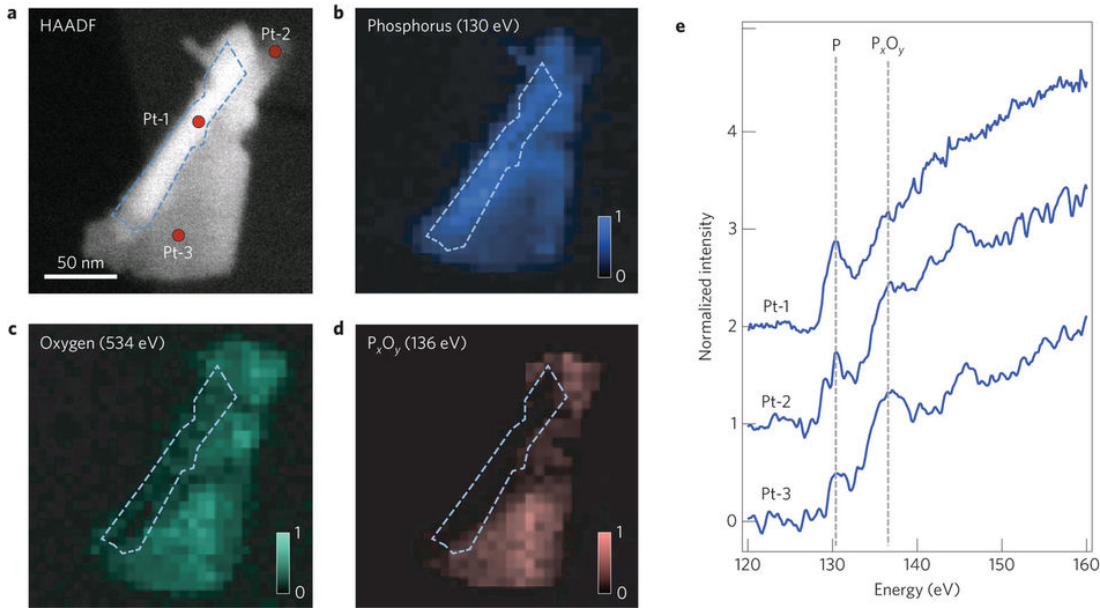
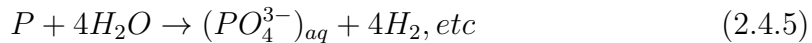


*Figure 2.11: Chemical analysis by hyperspectral TEM-EELS spectroscopy of a multilayer 2D-phosphane exfoliated under ambient light in air. a) High-angle annular dark-field (HAADF) contrast image taken at 80kV. b-d) EELS images extracted from the data cube at the energy of phosphorus L<sub>2,3</sub>-edge (130.2 and 136 eV) and oxygen K-edge (534 eV), as indicated. e) EELS spectra corresponding to the selected areas in a. Colour scale bars: normalized intensity relative to the maximum. [23]*

or



but instead reacts exclusively with  $O_2$  in water and air.

Wang shows via DFT that  $O_2$  interacts with phosphorene at room temperature, and that water does not, however it can dissociate when the phosphorene is already oxidised [55]. This agrees well with experimental data suggesting that the proposed reaction of oxidation followed by removal of species via dissolving in water occurs. They also note that water can adsorb to the surface of phosphorene via hydrogen bonds, even though it does not chemically bond. This is supported by some experimental data, however does disagree with some.

## 2.4.2 Secondary oxidation mechanism

The other proposed mechanism of degradation is not dominant for mechanically exfoliated FL-BP, however it is noticeable for solvent exfoliated or capped BP and starts at the edges [45]. Hanlon finds that the photo-luminescence spectra of dispersed nano-sheets of BP does not change with time, which they correlate to a lack of degradation. It is possible therefore that the solvent 'protects' the nano-sheets. They also find that the smaller sheets degrade faster in the solvent, suggesting that the decomposition starts at the edges due to their smaller area. Coleman et al. do not comment on the smaller sheets also being thinner, so this potentially corresponds to previous work [23] suggesting that the degradation rate is exponentially dependent on the bandgap which scales with thickness.

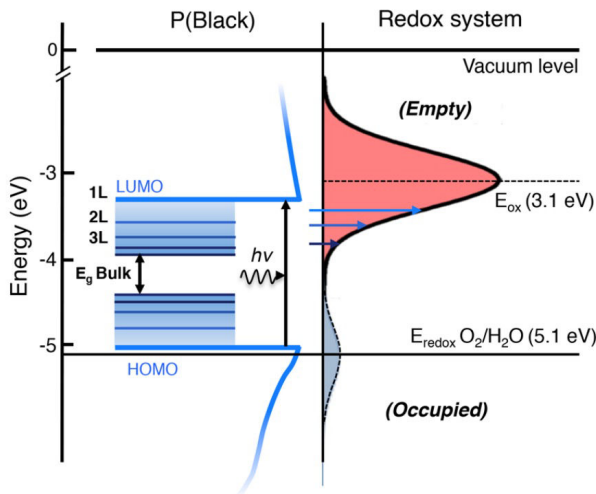
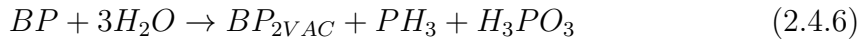


*Figure 2.12: Sketch of the density of states (DOS) of aqueous oxygen acceptor and of  $n$ -layer 2D-phosphane, as predicted by Marcus-Gerisher theory. On the left: DOS of mono-, bi- tri-layer 2D-phosphane and bulk P(black). On the right: the energy diagram of the DOS of aqueous oxygen acceptor states with the enlargement of the DOS due to the solvent reorganization. The figure also illustrates by the blue arrows the proposed CT reaction induced by photo-excitation of  $n$ -layer 2D phosphane. [54]*

The degradation pathway suggested is:



$BP_{2VAC}$  is a defective structure with two P vacancies in the BP super-cell. They find via considering the energies involved of forming BP vacancies that the reaction is exothermic at the edges and endothermic on the basal plane. Calculations show that BP can react with water via this mechanism. It is possible this reaction is extremely suppressed, as experiment shows deionized (DI), de-aerated water does not degrade BP [11].

## 2.5 Synthesis and Modification

Here the methods of synthesis for BP and phosphorene are discussed, as well as modifications of BP.

### 2.5.1 Black Phosphorus

BP can be produced via vapour phase deposition of red phosphorus onto catalysts of tin and tin iodide. The red phosphorus, tin and tin iodide are sealed in a glass ampoule in an inert atmosphere, then slowly heated and cooled in a controlled manner. These crystals grow into needle-like formations, with the long axis along the [001] (armchair) direction [56].

### 2.5.2 Phosphorene

The weak interlayer interaction in BP allows exfoliation via several methods. As with other 2D materials, the main two types of exfoliation are mechanical and liquid-

phase. BP is difficult to grow epitaxially, however one group has reported this as will be discussed.

### 2.5.2.1 Mechanical

Black phosphorene is exfoliated mechanically using a small variation on the usual technique [4]. The usual method of adhesive tape left adhesive on the surface and gave a low yield. An intermediate viscoelastic surface to exfoliate the flakes increases the yield and reduces the contamination of the flakes, the process is shown in figure 2.13.

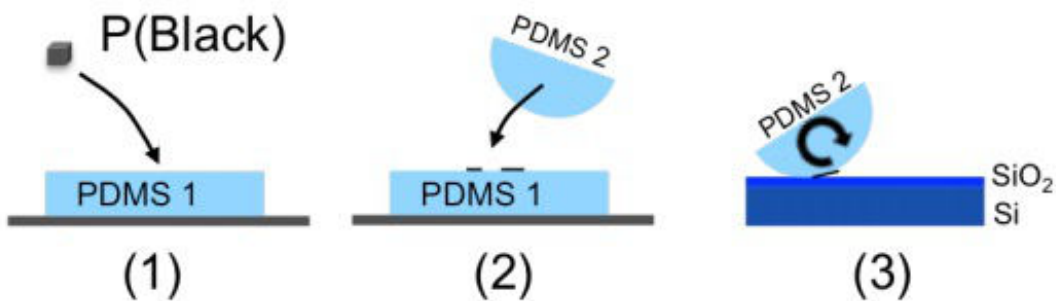


*Figure 2.13: Three step exfoliation procedure of P(black). Step 1: Exfoliation done on the flat PDMS-1. Step 2: The flakes were reported on semi-spherical PDMS-2 stamp. Step 3: the stamp was rolled on the substrate (SiO<sub>2</sub> on Si) with an estimated speed of 0.1 cm/s. [54]*

### 2.5.2.2 Liquid-Phase

The Coleman method involves grounding up BP crystals and mixing with high boiling point solvents such as CHP or NMP (other solvents have also been tried) [45]. These mixtures are then ultrasonicated, sheer mixed or sonicated to produce dispersion of nanosheets. TEM confirms that a bimodal distribution of widths is found (see figure 2.14) of 100nm and 3μm, with a mean thickness of 9.4 layers for BP. In IPA the mean length is around 1μm,. The dispersions can also be filtered through alumina membranes to remove larger flakes, this is confirmed with Raman and SEM [45].

Liquid-phase exfoliation using the Coleman method by Sun et al. showed that clean cut edges are present on exfoliated phosphorene along the ZZ long axis [31]. They see nano-belt objects, microns long, which are wide but have ribbon like aspect ratios.

Woomer et al. [13] used a similar technique, but instead utilised low power bath sonication. They then centrifuged to remove unexfoliated BP, and utilised further dialysis purification to remove small BP fragments. They claim this method can give thin phosphorene flakes of lateral dimensions up to 50μm, however no value for the thickness of these large sheets is given. The data indicates that above 120g centrifugation they appear to get no flakes with linear dimensions larger than 3μm.

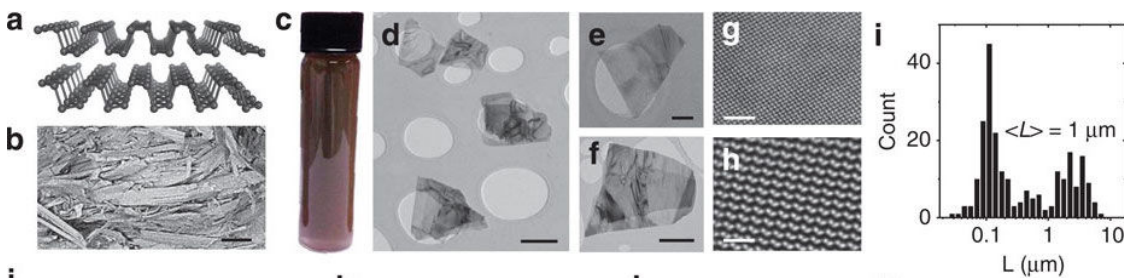


*Figure 2.14: Basic characterization of exfoliated black phosphorous. (a) Structure of black phosphorus (BP). (b) SEM image of a layered BP crystal (scale bar, 100 nm). (c) Photograph of a dispersion of exfoliated FL-BP in CHP. (d-f) Low-resolution TEM of FL-BP exfoliated in CHP (scale bars d-f: 500, 100 and 500nm). (g) STEM image and (h) HAADF STEM image of FL-BP (exfoliated in isopropanol) (scale bars in g and h, 2 and 1 nm). (i) Nanosheet length histogram of the exfoliated FL-BP from TEM (sample size=239). [45])*

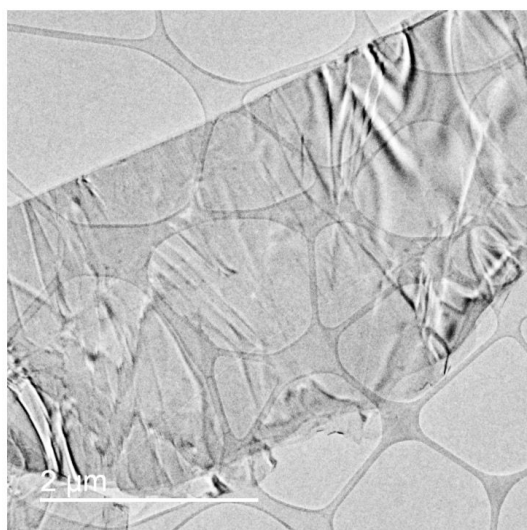


*Figure 2.15: TEM image of phosphorene nanobelt. [31]*

### 2.5.2.3 Growth

Thin film growth has been achieved by growing a thin film of red phosphorus, and then applying pressure to induce a transition to black phosphorus, yielding a film of thickness 40nm (which may potentially be improved to 5nm) with grain sizes of the order of 10nm [57]. The drawback of this technique is that the reported domain size is much smaller than that from other techniques.

### 2.5.2.4 Etching

Pei et al. utilised the stable oxide on BP by developing a technique to produce monolayer phosphorene using an oxygen plasma [58]. They use this plasma to oxidise the surface, and then etch the oxidised BP away, this results in a stable rate of etching and leaves a thin (11nm) layer of oxide on the surface. They show this can be used to engineer defects by over-etching the surface, and allow controllable production of few-layer BP, with small changes in PL and Raman intensities, although their techniques were not rigorous enough to prove that the monolayers behaved as pristine BP.

### 2.5.2.5 Modification

Hembram et al. used DFT to study the sodiation mechanisms in BP [34]. The key finding of this study was that sodium atoms prefer to intercalate into BP up to  $Na_{0.25}P$ , where they first preferentially intercalate into the same layer, then once covering 25% of each phosphorene layer they intercalate into other layers. This causes an interlayer expansion of  $2.26\text{\AA}$  to  $6.84\text{\AA}$ . In plane bonds show little change, neither do staggered bonds.

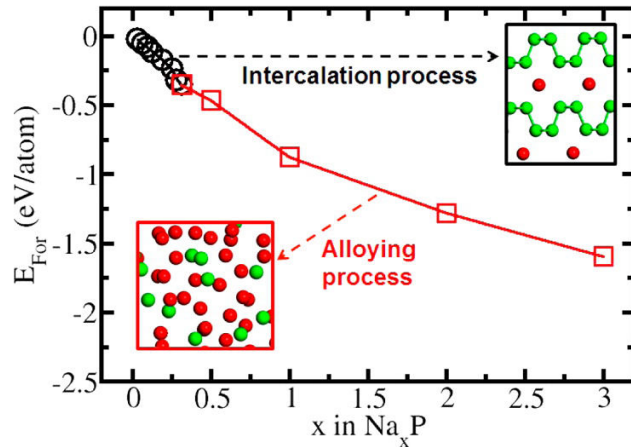


Figure 2.16: The results of DFT calculations suggest that above a 1:4 M:P ratio for sodium intercalation an alloy starts to form [34]

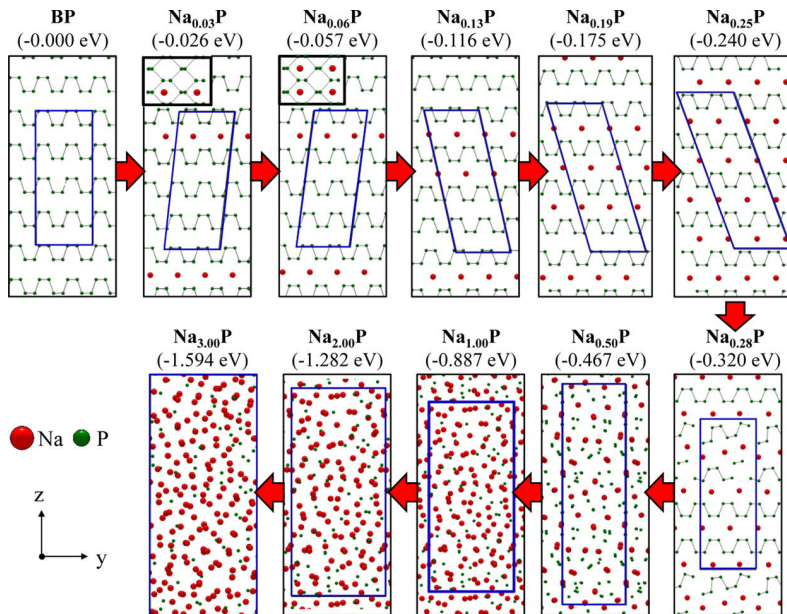
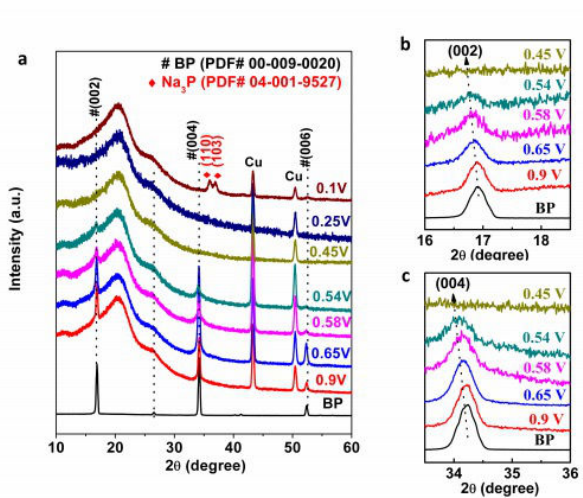


Figure 2.17: A sodiation mechanism of black phosphorus. Here, the numbers in parentheses indicate calculated formation energies of  $Na_xP$  structures. The blue solid lines indicate cell sizes of  $Na_xP$  including 64 P atoms used in our DFT calculations, and the black insets in  $Na_{0.03}P$  and  $Na_{0.06}P$  structures show top views of each structure to clarify positions of Na atoms in the structures. [34]

They found that intercalation above this ratio leads to alloying of BP. The stag-

gered bonds are longer and require less energy to break, additionally in intercalated BP increasing the interlayer distance leads to lower steric hindrance in the stacking axis, and also phosphorene layers begin to slide over each other generating lateral stress in the staggered bonds. This means that intercalated BP is easier to break p-p staggered bonds than in pristine. When these bonds break, there is predicted to be charge transfer from the Na atoms to the p-p dumbbells which are formed. They also see symmetric charge accumulation on the p-p bonds in BP which are unbroken nearby.

These studies have also been run for lithium and magnesium, but are not discussed here. There is little work on experimental modification of BP, however some electrochemical intercalation has been performed with sodium [31], some surface doping/intercalation has been done with lithium and made use of GIXRD and ARPES [59], additionally tellerium doped BP has been produced during growth of the crystals [60]. It is understood that work is also being performed on Ca and K doped BP via the metal-ammonia route, which is of interest due to potentially superconducting properties.



*Figure 2.18: Ex-situ XRD patterns of black phosphorus taken before charging and after charging down to different voltages. a) In wide range. b) Amplification of (002) diffraction peaks. c, Amplification of (004) diffraction peaks. [61]*

## 2.6 Applications

A wide range of applications for BP have been suggested and applied, BP has a huge range unusual and tuneable properties which makes in extremely interesting for 2D material devices (see figure 2.19). These range from optical applications such as saturable absorbers and thermal imaging sensors, to electronic applications such as radio frequency transistors. Other applications related to energy focus on the use of BP as sodium-ion battery anodes, solar cells and photo-catalysis.

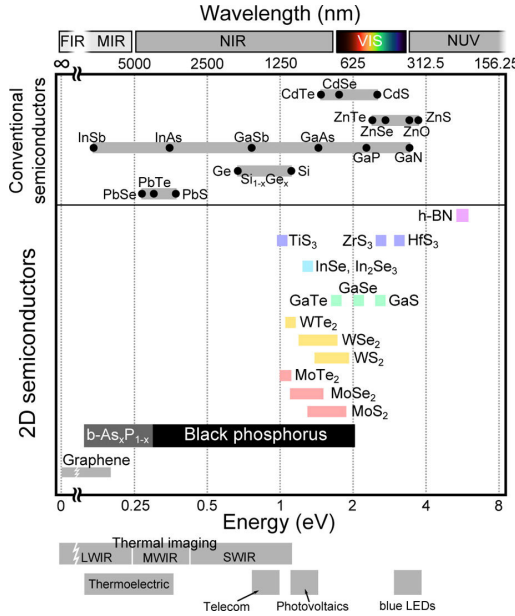


Figure 2.19: Comparison of the band gap values for different 2D semiconductor materials and some bulk semiconductors. [2]

## 2.7 Phosphorene Nanoribbons

Black phosphorus nanoribbons have been experimentally isolated via two methods. One production of the ribbons were actually macroscopic and too large to have the quantum confinement effects associated with the predicted unique characteristics. The second production described a method of making them, and confirmed they were structurally intact via TEM, although they were unable to measure any of the interesting properties yet. For this reason the many characteristic of BP nanoribbons are based on theory only.

Here we discuss the methods of production, the predicted properties and a discussion of specific applications of these ribbons.

### 2.7.1 Isolation

Lee et al. produced phosphorene nanoribbons via a top-down procedure [62]. They first mechanically exfoliated BP layers, and then used electron beam lithography (ELB) to cut them to dimensions. They then connected contacts via further ELB and ion milling to measure the thermal and electrical transport properties. They only achieved nanoribbons of 50nm thickness, due to difficulty in using a micro-manipulator in order to perform measurements. Furthermore, the ELB method was not precise enough to manufacture very thin ribbons, so the widths of the ribbons were of the order of over 500nm.

Das et al. utilized STEM beams in order to produce a 'lattice' of nanoribbons [20]. They first drill two holes in a BP flake using STEM, then etch away the area between them until a narrow region is left. This region can be selected as AC or ZZ and ribbons on the nm scale are formed, with edge roughness of the order of 1-2nm. These nanoribbons had widths of order 5nm and lengths of order 5-10nm

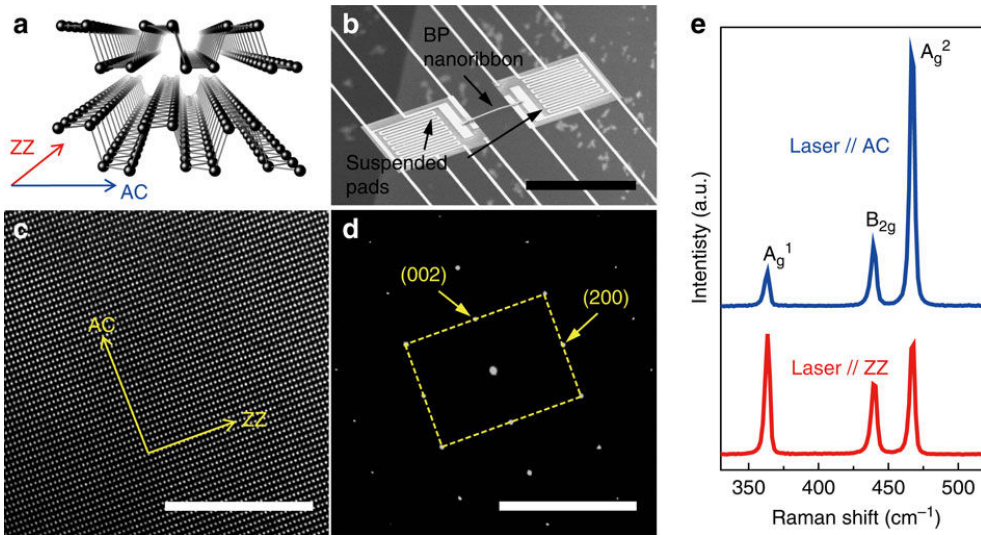


Figure 2.20: Crystal structure of BP and device structure for the thermal transport experiment. (a) Illustration of the crystal structure of BP ZZ and AC correspond to the [100] and [001] directions, respectively. (b) SEM image of a micro-device. Thermal conductivity is measured by transporting heat from the heated pad to the other pad through the nanoribbon. (c) High-resolution TEM lattice image of a BP flake. (d) SAED pattern taken from the area shown in c. (e) Micro-Raman spectra of a BP flake with laser polarized in parallel to the ZZ and AC axis, respectively. Scale bars, 50mm(b); 10nm (c); 20nm-1 (d). [62]

(until joining onto the larger lattice). No measurements on their properties were carried out, and it is unclear if they will behave as predicted. They also perform DFT to explain pore expansion within the flake once a hole is drilled, which expands preferentially along the AC direction.

## 2.7.2 Properties

Here the properties of BP nanoribbons (BPNRs) are discussed, focusing on the physical, electronic and optical and phononic and thermal properties.

### 2.7.2.1 Electronic and optical

There are a range of DFT papers predicting the possible properties of BP nanoribbons, however many disagree on the quantitative descriptions [3, 17–19, 21, 22, 40, 63–70]. They generally agree that with decreasing ribbon width, the band gap increases [71]. For very narrow ribbons (some changes predicted below 3nm, some below 10nm), researchers predict that ribbons of orientation zig-zag edge will be metallic, and those of armchair edge will be indirect semiconductors, however both can be made direct semiconductors by hydrogen passivation - a calculation backed up by multiple studies.

Nourbakhsh et al. found that due to the flat band structure in ZPNRs, optical transitions are forbidden near the gamma point [71]. This is because in optical transitions the dipole selection rules ensure that for a one photon transition  $\Delta L = \pm 1$  and the parity must be even overall.

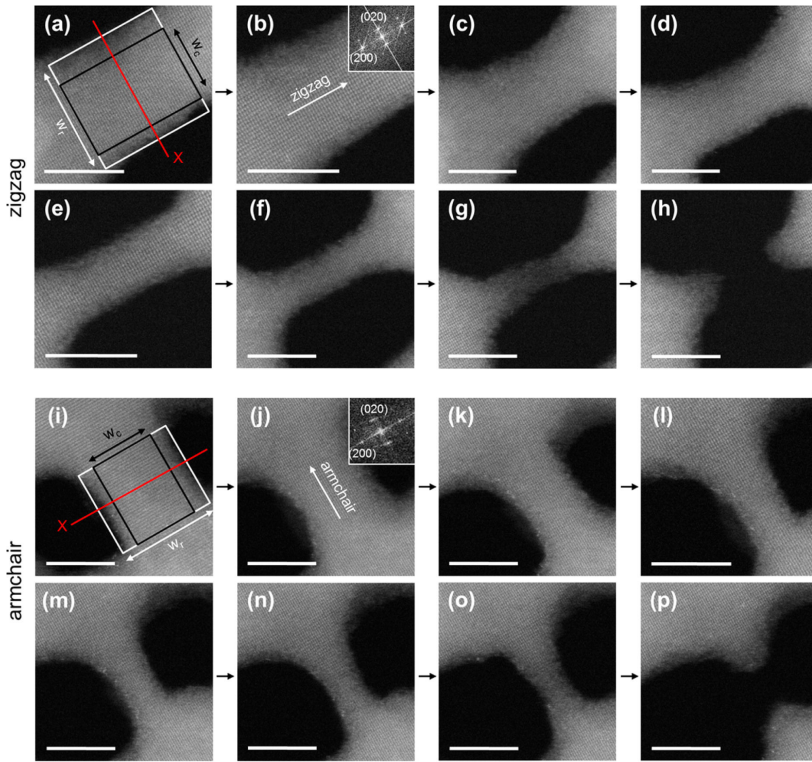


Figure 2.21: STEM nanosculpting of zigzag and armchair few-layer BPNRs. HAADF STEM images of an (a-h) 8.0 nm long zigzag and (i-p) 6.5 nm long armchair nanoribbon. [20]

Poljak and Suligoj investigated the immunity of electronic and transport properties of phosphorene nanoribbons to edge defects [64]. They note that for increasing the defects in PNRs, the DOS near the Fermi level increases due to edge states for both configurations of ribbon, and more Van Hove singularities away from the bandgap too. Also the variability from device to device increases with increasing defect density.

Zhang et al. calculated the formation energies for different geometry ribbons as a function of width [22]. A plot of these results is shown in figure 2.23.

### 2.7.2.2 Phononic and thermal

Lee et al. measured the electrical and thermal conductivities of their nanoribbons [62]. They note that BP has intrinsic anisotropy in its thermal transport and phonon dispersion. Nanoribbons of graphene exhibit similar anisotropy, however this is due to edge states causing different types of scattering depending on the edges, this effect may also be present in BP nanoribbons.

They also note that the Seebeck coefficient is slightly larger along AC (320 vs 270), and that the power factor ( $=S^2\sigma$ ) is three times as large along the AC vs the ZZ. This is due to higher electrical transport along AC. They also find relatively low ZT ( $\propto \frac{\sigma}{\kappa}$ ) values for these ribbons, but note they have single crystal ribbons with high  $\kappa$  and are undoped so low  $\sigma$ .

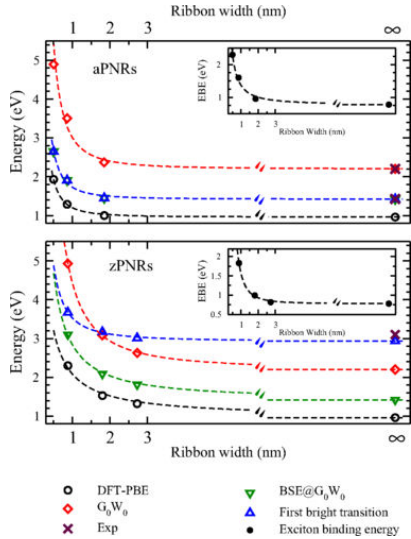


*Figure 2.22: The evolution of the band gaps (PBE, G<sub>0</sub>W<sub>0</sub>), optical gap (BSE@G<sub>0</sub>W<sub>0</sub>) and first bright excitonic state as a function of the nanoribbon width. The insets show the variations of the exciton binding energy (EBE) with the ribbon width. The power law fitting curves are presented by dashed lines. Experimental data of 2D phosphorene are marked by the cross sign [7, 27]. [71]*

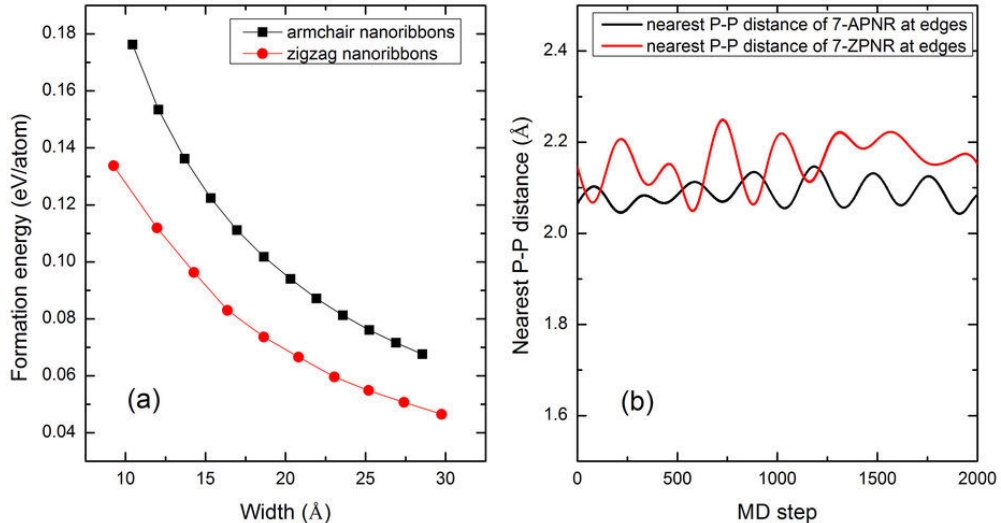


*Figure 2.23: (a) The calculated formation energy of APNRs and ZPNRs as a function of the ribbon width, and (b) the ab-initio MD results of the nearest P-P distance at the edges for the 7-APNR and 7-ZPNR at room temperature. [22]*

### 2.7.3 Applications

Zhang et al. found that the ZT value, which is an important measure for the effectiveness for thermoelectric applications, can be greatly enhanced for PNRs [22]. They used semi-classical Boltzmann theory, to deduce the thermal and electrical transport properties of ZPNRs and APNRs, as well as H-passivated edges. They found edge reconstructions in pristine ribbons, which caused indirect bandgap for APNRs and a metallic phase for ZPNRs unchanged. They did however see that H-passivation induced a direct bandgap in both types of ribbon.

They found that the ZT value in nanoribbons could be as high as 6.4 (which is comparable to current energy conversion methods), for n-type width 9 APNRs. H-passivated ZPNRs had the highest Seebeck coefficients and electrical transport, however they also had much larger lattice thermal conductivity, this lead to much smaller ZT values of 0.7 and 0.1 for p and n type respectively.

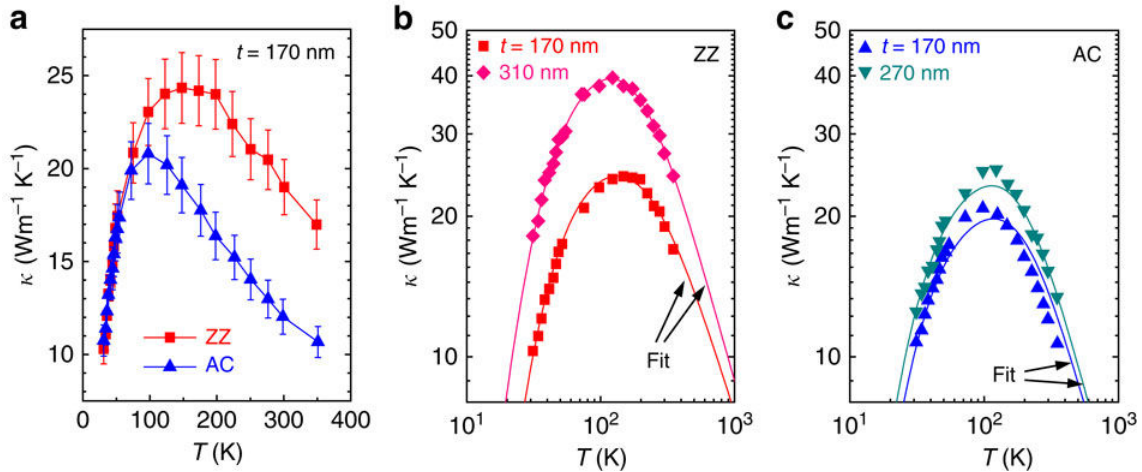


Figure 2.24: Temperature-dependent thermal conductivity of BP nanoribbons. (a)  $\kappa$  vs.  $T$  plot of BP nanoribbons axially oriented to the ZZ and AC directions, respectively. Thickness ( $t$ )/width ( $W$ ) of the ZZ and AC nanoribbons are 170/540 nm and 170/590 nm, respectively. (b)  $\kappa$  vs.  $T$  (logarithmic) of ZZ nanoribbons with different dimensions; 170 ( $t$ )/540 nm ( $W$ ) and 310 ( $t$ )/540 nm ( $W$ ). (c)  $\kappa$  vs.  $T$  (logarithmic) of AC nanoribbons with different dimensions; 170 ( $t$ )/590 nm ( $W$ ) and 270 ( $t$ )/420 nm ( $W$ ). Lengths of the nanoribbons all exceed 10 mm. [62]

Nourbakhsh et al. investigated the exciton fine structure (i.e. splitting) and found it is very large PNRs, and largest for narrow ZPNRs. This singlet-triplet splitting is larger than for systems such as carbon nanotubes, graphene and doped silicon nanowires which are usually considered impressive [71–74]. This has potential applications in PV, biomedical, photo-luminescence and quantum information.

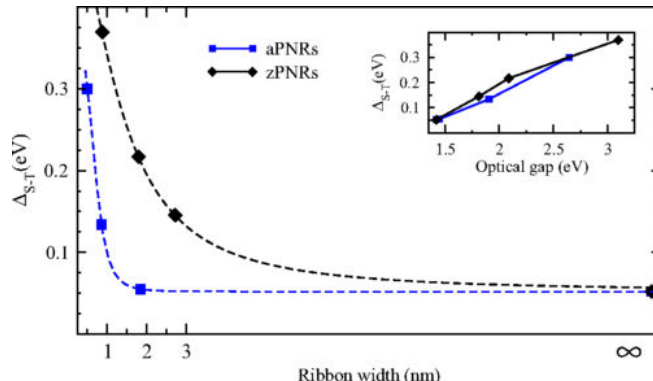


Figure 2.25: Exciton exchange splitting versus ribbon width. In the inset, the exchange splitting as a function of the band gap of PNRs. [71]

# Chapter 3

## Literature Review - Techniques

Here the theory of the main experimental techniques used is discussed.

### 3.1 Diffraction

When light (or any wave) passes a barrier, the waveform is modified at the boundary edge. If it passes through a gap then further distortion occurs, reaching a maximum for the gap the size of the wavelength of the wave, this is the process which is called diffraction. The diffracted light can be focused onto a screen, or detector, and the resulting image is called the diffraction pattern. For a periodic structure this pattern corresponds to the reciprocal lattice of the structure.

Bragg's law is the most fundamental equation used in diffraction theory. It describes the relationship between light and matter which is necessary for diffraction to be observed. In a perfect crystal the only constructive interference occurs for waves which have a path length which is a multiple of their wavelength. Since these waves are diffracted from planes of atoms in a crystal, Bragg showed that the distance between these planes,  $d$ , can be related to the wavelength via simple geometry to give the condition for constructive interference. In a large crystal all other angles of the waves striking the crystal are cancelled out. Bragg's law is:

$$n\lambda = 2ds\sin(\theta) \quad (3.1.1)$$

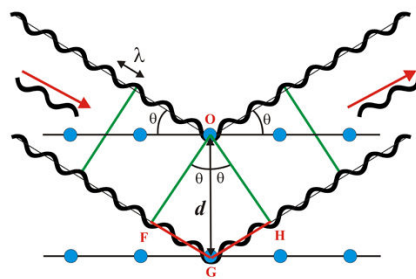


Figure 3.1: A schematic of Bragg's law

In general, we measure  $|A^2|$ , not  $A$  (can think of this as an energy density or quantum mechanically as  $|\psi^2|$ ). This leads to the 'phase problem', which is due

to the loss of information regarding phases, i.e. information about the location of atoms due to the square modulus.

Note that lenses essentially do a Fourier transform of light phases from diffraction centres without the loss of phase information, as the light is focused. This is why electron microscopes are of such use, as they allow us to directly image the atoms without the loss of information.

In a crystal, the scattering amplitude is:

$$A^{Crystal} = \sum_{k_n+r_j}^{All atoms} f_j e^{iQ \cdot (R_n + r_j)} \quad (3.1.2)$$

$$A^{Crystal} = \sum_{k_n}^{Lattice} e^{iQ \cdot R_n} \sum_{r_j}^{Unit cell} e^{iQ \cdot r_j} \quad (3.1.3)$$

The amplitude of scattering is determined by the unit cell structure factor:

$$F_{hkl} = \sum_{r_j}^{unit cell} f_j e^{iG \cdot r_j} \quad (3.1.4)$$

This means that the positions of the diffraction spots are due to the lattice, and the amplitude of each spot is due to the unit cell structure. Note the atomic form factor,  $f_j(Q)$  is dependent on Q for x-rays, and not for neutrons.

Fourier synthesis does an inverse FT on the structure factor to try to reconstruct the scattering density:

$$\rho(q) = \frac{1}{V} \sum_Q F(Q) \exp(-iQr) \quad (3.1.5)$$

But as we measure the intensity, not  $F(Q)$ , we cannot easily do this (phase problem). Fourier back transforming the scattered intensity that we measure gives  $g(r)$ , the pair correlation function (called the Patterson function for crystals). To calculate the phase we need information on the atomic positions, xyz, and so we need to build a model and then use the Patterson function (or direct methods).

## 3.2 TEM

The components of a TEM, the resolution, analysis and other notes are discussed below.

### 3.2.1 Components of a TEM

Electron microscopes work by first creating a stream of electrons, then making use of magnetic lenses to focus the beam into a monochromatic thin focused beam. They are then focused onto the sample and the resulting scattered electrons are imaged on a CCD in order to analyse the interaction. The different components are discussed here.

### 3.2.1.1 Gun and monochromator

There are two main types of electron gun, thermionic and field emission. Thermionic electrons are produced from a filament or from a sharp tip by field emission. The choice of gun is dependent on the price of the TEM, however field effect sources have higher currents, smaller spread of electron angles and energies. The electrons are then accelerated through a voltage.

A monochromator is often used to further increase the energy resolution for HRTEM, and is positioned before the accelerator.

### 3.2.1.2 The specimen

When electrons hit the sample there are a variety of interactions, the interaction volume represents the region which the electrons penetrate into (a larger incident energy increases the interaction volume). Different information can be deduced from different penetration depths, TEM is typically performed on samples less than 50nm thickness. TEM uses electrons that pass completely through the specimen, producing an image of the specimen from these electrons, similar to in transmission light microscopy.

Secondary electrons are produced in the 5-50nm range, electrons interacting the first 1nm are called Auger electrons. The Auger process is deenergization of an atom after a secondary electron is produced, which is when one is knocked out of its shell by scattering. Auger electrons can be used to identify the element. Xrays could also be produced if the electron falls down a level, and the energy of these electrons can also be used to characterise the elements present.

### 3.2.1.3 Condenser lenses

Condenser lenses are a series of magnetic lenses used in TEM's. They are equivalent to a convex optical lens and are usually made of copper wires wrapped around iron cores. They select the spot size and the intensity/brightness, and they also increase the spatial coherence of the beam.

Condenser lenses are essential to the focusing of a TEM beam, however they often produce a rotation of the image which must be corrected for. This is due to the helical trajectories of electrons in a magnetic field.

### 3.2.1.4 Objective aperture

The objective aperture is the aperture which chooses which part of the beam (post-specimen) is analysed. It can be positioned for bright field imaging, which is the type of imaging normally used in optical microscopes. Dark field imaging can also be used, where a single diffraction spot is imaged, and is at the outer edges of the beam imaged for bright field. A diffraction pattern can be obtained by imaging all of the beam post-specimen, see figure 3.2 for details.

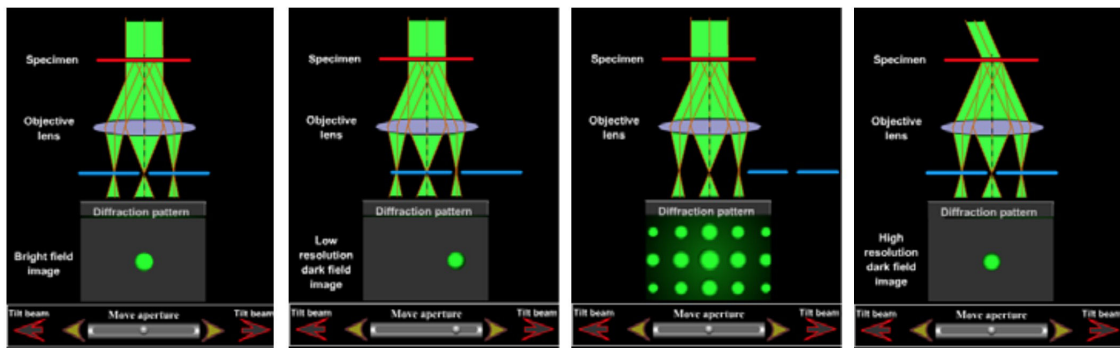


Figure 3.2: A schematic of the different objective aperture modes

### 3.2.1.5 STEM

STEM stands for Scanning TEM. This is when scattered electrons are detected by annular CCDs which are scanned over the image, whilst also measuring bright field transmitted electrons, see figure 3.3. This is a surface imaging technique, due to the detection of surface scattered electrons, it is therefore sensitive to impurities and solvents around the surface. Note that high angle annular dark field is usually used for this, as it detects over a range of elements and the scattering is related to the density of material (other modes can be used which are more sensitive to lighter elements).

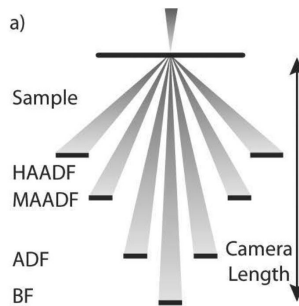


Figure 3.3: A schematic of STEM modes

## 3.2.2 Resolution

Diffraction is limited when focusing waves, as can be seen from the Rayleigh criterion:

$$\delta_d = \frac{0.61\lambda}{nsin(\alpha)} \approx \frac{0.61\lambda}{n\alpha} \quad (3.2.1)$$

where n is the refractive index of the material, alpha is the incident angle and lambda is the wavelength which is varied with accelerating voltage, therefore a higher voltage gives a better resolution. As wavelength becomes small aberrations become important, it is possible to get chromatic aberration due to wavelength spread, and spherical aberrations due to the uneven curvature for each radius.

The total beam size has both aberration and diffraction:

$$\delta_{total} \approx \sqrt{\delta_s + \delta_d} \quad (3.2.2)$$

The optimum value is when they are equal, which is  $\alpha^4 = 0.61\lambda/C_s$ , about 0.2nm in a good 200kv TEM.

Spherical aberrations are given by:

$$\delta_s \approx C_s \alpha^3 \quad (3.2.3)$$

Chromatic aberrations are normally not important except for thick samples.

### 3.2.3 Contrast

The phase and amplitude variations due to electron interactions can be used to produce contrast on the detectors. These variations can be due to a change in the mass of the sample, or due to changes in thickness's (also diffraction). The phases of electrons are shifted when passing through columns of atoms (unchanged when passing between columns) and so contrast can be formed here, this is dominant for high magnifications.

### 3.2.4 Analysis

When analysing a TEM image, it is important to take into consideration the setup of the TEM as discussed above, including the effects of contrast. It is possible using advanced techniques to get the thickness of a sample from the scattering of electrons from a sample. This requires very careful setup and analysis, and is usually reserved for HRTEMs.

When analysing TEM data, the material should be confirmed by both elemental characterisation techniques, as well as via diffraction. EDX and EELS data can be analysed using software packages, which will indicate the elements present. Advanced characterisation can tell more about the elements present, such as trends in band gaps or the type of bonding the electron had, however this usually requires very clean samples and well aligned, high end hardware.

Diffraction patterns should be indexed by using the spots present as lattice spacings. Reciprocal lattice points have size and shape in reality eg a disk of material makes a relrod in reciprocal space. The spacing of the spots can be found by:

$$\lambda L = d_{hkl} R_{hkl} \quad (3.2.4)$$

where L is the camera length, d is plane spacing and R is the spot spacing on a real negative in mm. Following calibration the following equation can be used:

$$R_{hkl} = \frac{\lambda L}{d_{hkl}} = \frac{1}{C d_{hkl}} \quad (3.2.5)$$

Where C is a calibration factor, so in practice images usually have  $d^{-1}$  equal to the distances measured on the spot after calibration is applied (i.e. we scale R by C).

A lattice vector joins any two lattice points, and can be expressed as:

$$t = Ua + Vb + Wc \quad (3.2.6)$$

or  $t = [UVW]$  (Weiss zone law).

If a lattice vector lies in a lattice plane ( $h,k,l$ ) then  $hU+kV+lW=0$ . Diffracting planes must be parallel to the beam, therefore they obey this law, and this can be used to find the 'zone axis' of the diffraction pattern.

To index the spots, the  $d$ 's found are matched with  $hkl$ 's for the crystal by looking at a list of the  $d$  spacings for each miller plane. Then, using the cross product, the zone axes can be found. If the EDX and diffraction pattern match as expected, then the material can be confirmed with confidence.

### 3.2.5 Other notes

Moire patterns are a type of pattern due to the overlapping of periodic images offset by an angle, and are general to all such structures. These can be seen when using polarising filters, and show up as interesting patterns. For thin crystalline samples, this can also be seen as the periodic columns of atoms overlap, and can be useful to confirm that periodic crystal structures are turbostratically stacked. A FFT of an image with Moire patterns can give the rotations of these layers.

Beam damage can often occur in samples due to the interaction of high energy electrons with the sample. This is much more pronounced for thick samples, and also for samples with some adsorbed solvents. In the latter case boiling of the solvent can often be seen when imaging. If the crystal sample itself is damaged by the beam, then destruction of the lattice whilst imaging may be observed. Note damage may be formed by : knock-on damage, sputtering, phonon creation (especially for low thermal conductivity samples) and radiolysis.

## 3.3 AFM

AFM is a technique which allows the direct measurement of height and works by rastering a sharp tip across a surface, the tip is deflected by surface forces depending on the mode. This deflection can be read out and produce nm resolution topographical maps of a material.

### 3.3.1 Types

There are several types of AFM which are frequently used, and will be discussed here. The main distinction is between those that do and do not use feedback loops to control a parameter.

### 3.3.1.1 Contact

The original AFM device was based on what is now called contact mode AFM. This works by rastering a tip over a surface in contact and measuring the deflection of the tip with a laser diode. The tip acts as a spring, and by Hooke's law the deviation can be deduced from the deflection.

Contact mode is advantageous for faster scanning and also for more accurate measurements on samples with extreme height variations. The disadvantages are that it can be distorted by lateral forces, and strong capillary forces from liquid layers can damage the sample and or tip.

### 3.3.1.2 Tapping

Another mode which is often used for more delicate samples is intermittent contact mode. This works by oscillating the tip in order to deduce the forces acting on the tip. Tapping mode works by oscillating the cantilever slightly below its resonant frequency, and as it nears the surface the forces acting on it change. These changes in force affect the resonant frequency of the cantilever via the following relation:

$$\omega = \omega_0 \sqrt{1 - \frac{1}{k} \frac{dF}{dz}} \quad (3.3.1)$$

and so the resonant frequency is dependent on the distance from the surface. Also note that the damping changes near the surface. By monitoring the amplitude of the oscillation, the resonant frequency of the tip can be monitored and so the distance from the surface deduced. This is usually done by attempting to keep the amplitude constant by adjusting the height, thus giving a topographical map.

Forces cause the attraction of the tip to the surface when it is near, at some point this can cause the tip to snap to the surface. If liquids are present on the surface then capillary forces may cause a larger force than originally detected when the tip is withdrawn. This is particularly import in peak force tapping mode.

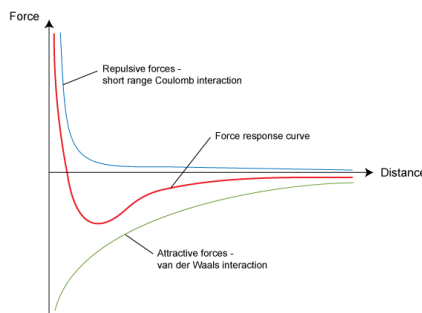


*Figure 3.4: A schematic of the force-distance curve for the interaction of the tip with the surface*

The advantage of this method is that lateral forces are not significant, there is greater lateral resolution on samples and also less damage to the sample. This mode is much slower than contact mode, though.

### 3.3.1.3 Non-contact mode

In non-contact mode, the cantilever oscillates near the surface without touching it, the oscillation is just above the resonant frequency. Van der waals forces near the surface cause a decrease in the resonant frequency and thus an decrease in amplitude of oscillation. This mode is particularly affected by surface liquid and so is usually used under UHV conditions.

This mode is very good for soft samples and lateral and normal forces are greatly reduced, and atomic resolution can be achieved in the right conditions. The scans speeds are however, much slower, and the liquid layer can ruin measurements.

### 3.3.1.4 High speed AFM

High speed AFM works by directly using a force feedback in contact mode AFM. This means that, with some sophisticated piezo techniques and analysis, that frame rates up to kHz can be achieved, substantially reducing the time needed to scan an area. This allows for large area scanning to be performed, whilst causing minimal damage to the sample due to a lubricating effect.

## 3.3.2 Artefacts

Artefacts can be caused by many things in AFM, the possible causes are discussed here.

### 3.3.2.1 Scanner/piezo

The piezoelectric response to voltage changes is not linear, and hysteresis in the piezo can mean that incorrect height changes are measured. This can be corrected for with proper calibration, using a non-linear voltage change for height adjustment.

Due to the nature of the scanner head, it often does not move in a flat plane, but rather on a bowed surface. The scanner may also not be parallel to the surface being scanned, resulting in tilt. These effects can be removed with software.

Scanner creep can also be an issue due to sudden voltage changes on the piezo.

### 3.3.2.2 Tip

The shape of the tip can often be an issue for AFM, for example a blunt tip can measure objects as wider than they are.

The tip can also pick up debris during a scan, leading to many artefacts on the height measurements. This can be checked by rotating the sample by 90 deg.

### 3.3.2.3 Feedback

Feedback errors are caused in looped systems where there is a delay between a change and an adjustment to the setpoint. For example in tapping mode this can result in an amplitude error as shown in figure 3.5.

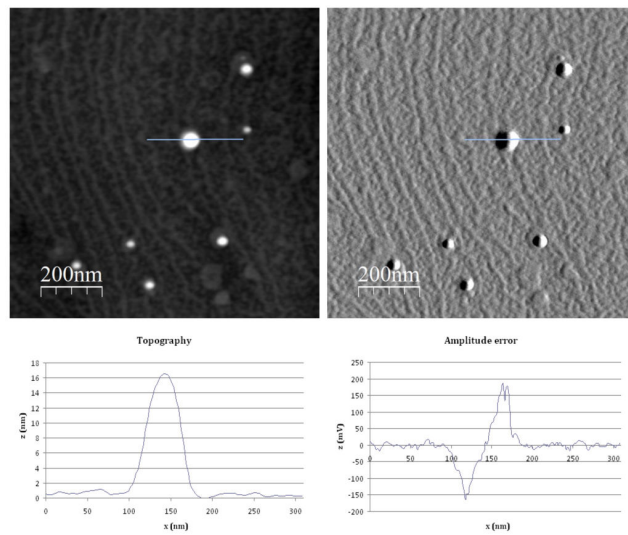


*Figure 3.5: A schematic showing the relationship between amplitudes and errors due to feedback loops.*

### 3.4 XPS

X-ray Photo-emission Spectroscopy (XPS) is a technique which utilises the photo-electric effect in materials. It works by bombarding a sample with low energy x-rays, and then measuring their kinetic energy upon detection. The binding energy of the electron can be found via:

$$E_K = h\nu - \phi - E_B \quad (3.4.1)$$

Where  $E_K$  is the kinetic energy of the electron emitted,  $h\nu$  is the energy of the x-rays bombarding the sample,  $\phi$  is the work function of the instrument detector and  $E_B$  is the binding energy of the electron emitted from the sample.

The emitted electron is from core levels and the binding energy gives clues about the chemical environment of the atom upon emission. Note this is a surface sensitive technique and electrons from deeper than  $100\text{\AA}$  are rarely detected.

# Chapter 4

## Methodology

Here the experimental methods which lead to the production of black phosphorus nanoribbons are discussed.

### 4.1 Metal-Ammonia solutions

Upon addition of an alkali metal (and some other species not discussed here), the electron is liberated from the metal in the following manner [75]:



This equation is at the heart of these solutions, there are essentially two regimes for metal-ammonia solutions; 1 - a dilute phase where the electron is solvated by ammonia molecules 2 - a concentrated phase where the electron is dissociated from the metal completely, and the solution acts like a metal [75, 76]. We are interested in the dilute phase for reduction of layered materials.

When a Van der Waals crystal is added to a metal-ammonia solution, we expect the solution to reduce the crystal. This may result in intercalation, as in graphite and some other layered materials, or may result in a breakdown of the crystal. In graphite the end point of this reduction is clear ammonia and a reduced graphite crystal, since the solvated electrons have been transferred to the crystal. This charge transfer results in negatively charged graphene layers with positively charged anions between the layers and will act as a salt (note this may depend on ammonia pressure and staging) [77, 78]. This results in wider separation of the layers, thus reducing the Van der Waals forces, however also results in an increased force between the layers due to electrostatics. Interestingly, in graphite systems this can sometimes result in ammonia also being present within the galleries, with a resultant 2D metal-ammonia solution between graphene layers (for ammonia over-pressure only).

When the reaction has finished, the ammonia must be removed slowly, so as to avoid damage to the crystals from rapid boiling of ammonia.

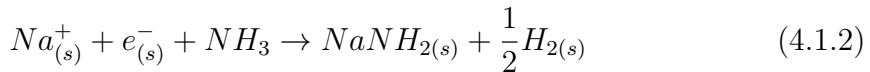
#### 4.1.1 Decomposition

Metal-ammonia solutions are metastable, and so it is expected that decomposition will continually occur within these solutions. There are several factors which can

affect the rate of decomposition [75]:

- Impurities
- Electron scavenging
- Temperature

The decomposition reaction is as follows:



The rate of this reaction increases with temperature, and so keeping these solutions cool is imperative.

Impurities only act to increase the rate of this reaction, as they act as catalyst sites, it is therefore important that all materials involved in the production and use of these solutions are thoroughly cleaned. For ammonia this can be achieved by dissolving ammonia onto mechanically cleaved metal, and then, after several hours, cryo-pumping the ammonia back into a lecture bottle. The ammonia, when frozen, can then be pumped on to remove any hydrogen which will still be gaseous at liquid nitrogen temperatures. This produces amides which dry on the glassware and can then be washed away. This method can also be used to clean glassware. Glassware can hold 'electron scavenging sites' due to metal atoms, water or radicals which also catalyse the reaction shown in equation 4.1.2 [75].

It is important to avoid decomposition when studying or using these solutions, as this will skew the concentration measured. There is also the issue of gas evolution, which can be potentially explosive if appreciable decomposition occurs in a sealed container.

## 4.2 Dissolution/suspension

2D materials have often been considered using DLVO theory, applying the ideas developed for colloids to these novel systems. This probably is not a good description, and some of the basic theory is outlined here and the potential misuse of this theory briefly discussed. The ideas behind spontaneous dissolution, and the advantages of this over conventional approaches are discussed.

### 4.2.1 Overview of DLVO

DLVO theory seeks to quantitatively describe the interactions in solutions. It accounts for both the van der Waals forces and the repulsions due to electrostatics and the electrical double layer. The total potential due to interactions is given by:

$$V_T = V_A + V_R + V_S \quad (4.2.1)$$

Where  $V_T$  is the total potential between particles,  $V_A$  is the attraction due to van der Waals forces,  $V_R$  is repulsion due to the electrical double layer, and  $V_S$  is

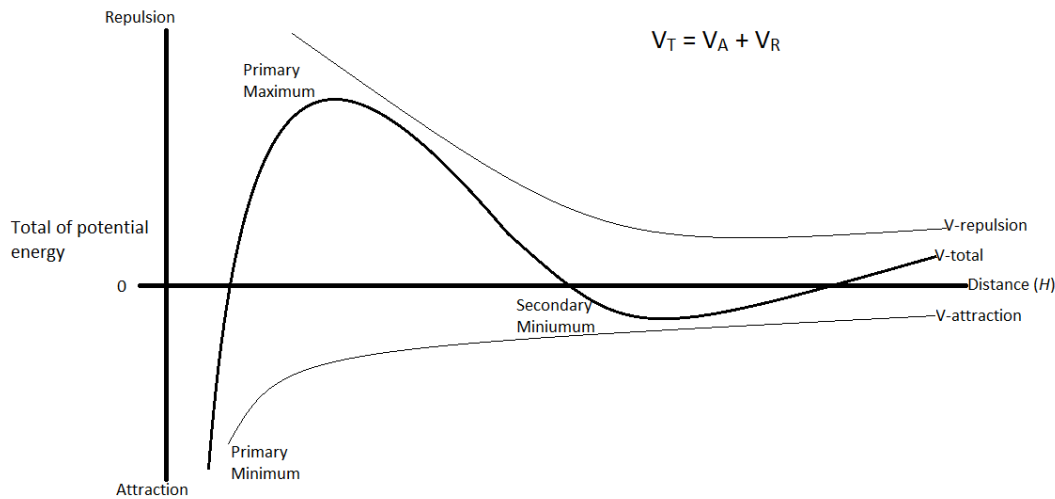


Figure 4.1: The variation of attraction/repulsion with distance for two particles described by DLVO theory [79].

the repulsion due to steric effects.

The combination of electrostatic repulsion and attractive forces leads to a potential barrier to be formed, as long as this is above the thermal energy of the solute constituents then it will prevent re-aggregation. Electrolytes compress the double layer, thus decreasing the primary minimum and deepening the secondary minimum, thus increasing the tendency for flocculation.

DLVO is based on additivity of the forces involved in suspension of objects in solvents. For 2D materials this is an inherently flawed idea, since the forces involved are interrelated, and so cannot be simply added [80]. The low dimensionality of these objects also means that solvent ordering is essential to explaining the stability of 2D materials in solution, and so theories which ignore this ordering will give poor descriptions of the solvation [81].

In any description, it is essential to consider the Gibbs free energy change upon dissolution, given by:

$$\Delta G = \Delta H - TS \quad (4.2.2)$$

If this is positive upon dissolution then this indicates stability, and if negative it indicates that re-aggregation will occur.

### 4.2.2 Spontaneous dissolution

Traditionally researchers have attempted to overcome the interlayer bonding in layered materials by physical or chemical methods [82–84]. These methods are usually aggressive and lead to uncontrollable damage of the material, and produce dispersions of the 2D material [85].

As mentioned, the use of metal-ammonia solutions may act to produce charged

layers with anions between the layers . If this does occur, then the distance between layers will be increased, however the electrostatic forces introduced will likely overcome any decrease in interlayer bonding [86,87]. It is therefore expected that spontaneous dissolution will occur due to energy changes upon solvent reorganisation. The rate of dissolution will likely be limited by the size of the flakes which dissolve.

Note that if there is not charge transfer, and the sheets of the material are not charged then this is not expected to occur. However, in this regime the interlayer interaction will be reduced overall due to widening of the layers with no electrostatic interaction to counter this. It is possible if degradation occurs in the galleries then this could be the result.

#### 4.2.3 Suspensions vs solutions

Once the 2D material is separated from the bulk it must then be suspended in a solvent to be dispersed. This is often done using methods such as surfactants or functionalisation or in this case, charging [85,88,89]. By using the method of spontaneous dissolution by alkali metal doping, we aim to charge the sheets and produce a stable solution due to solvent reorganisation. For this reason polar solvents are used, and they are also chosen to be aprotic to reduce reactivity.

The dispersed 2D materials in this scenario are truly in solution, and are not a metastable dispersion as for methods such as sonication [87]. This is not necessarily essential, as many applications of 2D materials from liquid phase exfoliation can still be realised in dispersion, however more gentle methods allow less damage to the 2D material and have longer shelf-lives.

The use of Hansen solubility parameters is often discussed, however this is known to not give a full description of the solvent interaction, it can predict some good solvents for 2D materials. It is an empirical description which matches surface energies of 2D materials to solvents.

# Chapter 5

## Research question

The research aim for this project is to obtain a reliably reproduceable, and controllable film of 2D phosphorene by using the intercalation followed by liquid phase exfoliation. Characterisation techniques are used on the solution and the intercalant in order to measure the success of these processes.

As the project progressed it became evident that an unexpected production of phosphorene nanoribbons had occurred. The aim has thus shifted to fully understand the process and characterise the ribbons and materials at all stages. The current work demonstrates the first known isolation of black phosphorus nanoribbons, and has been produced using a method which can be potentially scaled to industrial application. The process is still far from being fully understood and controlled, however production of isolated nanoribbons is extremely novel in this field and is thus the focus of this project.

Current work has lead to the current stage of progress which is almost ready for publication, future work will focus on theoretical simulation of stages of this process, as well as a parallel project which will depend on the formation of glasses of metal-ammonia solutions -which is not discussed in detail in this report.

# Chapter 6

## Work so far

The work undertaken so far has mainly focused on production and characterisation of black phosphorus nanoribbons. Here this work is summarised, and other work undertaken is also briefly summarised.

### 6.1 Nanoribbons

The production of nanoribbons is a two stage process. First the bulk crystal is intercalated, and then dissolved in an aprotic non-polar solvent with mild agitation, via bath sonication or stirring. Here work which confirms intercalation is presented, and then evidence of successful exfoliation is also presented. Future work which focuses on characterisation of the nanoribbons and understanding of the mechanism is also described.

#### 6.1.1 Evidence of intercalation

Metal-ammonia reduction has been performed on black phosphorus crystals obtained from Smart elements (99.9% purity) or Andrea Sella (unknown purity). It has been performed with sodium and lithium with varying stoichiometry. Here the XRD patterns of the reduced crystals are shown for each metal, and compared to known crystal structures for decomposition products.

##### 6.1.1.1 Visual evidence

During the metal-ammonia reduction, involving either lithium or sodium, there are distinct colour changes observed which differ from those expected with typical reductions. When a dilute metal-ammonia solution is produced, a dark blue colour is expected. This colour is due to a confined electron, and is the result of optical transitions of this electron. When black phosphorus is added to these solutions, a green colour is often observed. Following this a clear orange colour is observed toward the end of the reduction. At this stage a clear colour is usually expected, due to charge transfer of the confined electrons to the layered material (along with intercalation with a metal ion). Once the liquid ammonia is removed an orange residue is left over, and during removal of ammonia the orange colour of the solution becomes more intense. This suggests that the orange colour is due to dissolved species, and the leftover residue is the solid form of these species. Figure 6.1 shows these stages

of the black phosphorus reduction.

The black phosphorus crystals do not appear to dissolve well in ammonia, and so in future work subsequent ammonia dissolutions will be used in order to separate the byproduct from the bulk black phosphorus crystal. Literature on these systems is sparse, however some notable work on white and red phosphorus suggests that these brightly coloured compounds are metal phosphides [90, 91], with a rich variety of potential structures formed depending on reaction conditions. Interestingly, ammoniated phosphides can be formed from these reactions, however similar reactions are observed in THF and other organic solvents. This may suggest that improper removal of these phosphides from the bulk crystal before dissolution in organic solvents may lead to further reactions/products to be formed. This can lead to degradation of the solvent and residue upon removal of the solvent. This has been seen for solutions which give more phosphide left on the surfaces of the crystals, however it has yet to be tested with complete removal of the phosphides. This may lead to easier drying and therefore better results for TEM and AFM analysis.

#### 6.1.1.2 Xray diffraction of intercalant

XRD of the reduced crystals is poorly reproducible, with different changes in structure between samples prepared with identical conditions, and also with different parts of the crystal appearing to have no change in structure. This may suggest that the production of phosphides and of intercalated crystal are competing processes, and minor changes in conditions can lead to drastically different phosphide species being produced. Additionally, the phosphides seem to be produced at the surfaces of the crystals, and the variation in structure within the same crystal may also suggest that intercalation occurs primarily at the surfaces first, as seen in graphite and other layered materials. To counter this, the amount of phosphide produced should be reduced, and metal-ammonia reduction run for much longer timescales, as tested for  $MoS_2$  [92].

The XRD patterns ex situ are shown in figures 6.2 and 6.3. Lithium-ammonia solutions produce a phase which has new, broad peaks at high d spacing. This d spacing could correspond to an expansion of the stacking axis of up to triple its original size, this may be due to expansion of layers (potentially with phosphides being produced in the galleries), or due to staging or alteration to the structure such as sliding of the phosphorene layers upon intercalation, thus increasing the unit cell size.

When sodium is used there are two new very sharp peaks on the diffractogram. The origin of these peaks is not obvious, and has not been reproduced yet, potentially suggesting a contaminant in the original test.

The rich range of non-ammoniated phosphide structures have been compared to these diffraction patterns, however there does not seem to be any obvious appearance of these phases. Furthermore, the extremely wide range of peaks for these structures makes assignment somewhat meaningless.

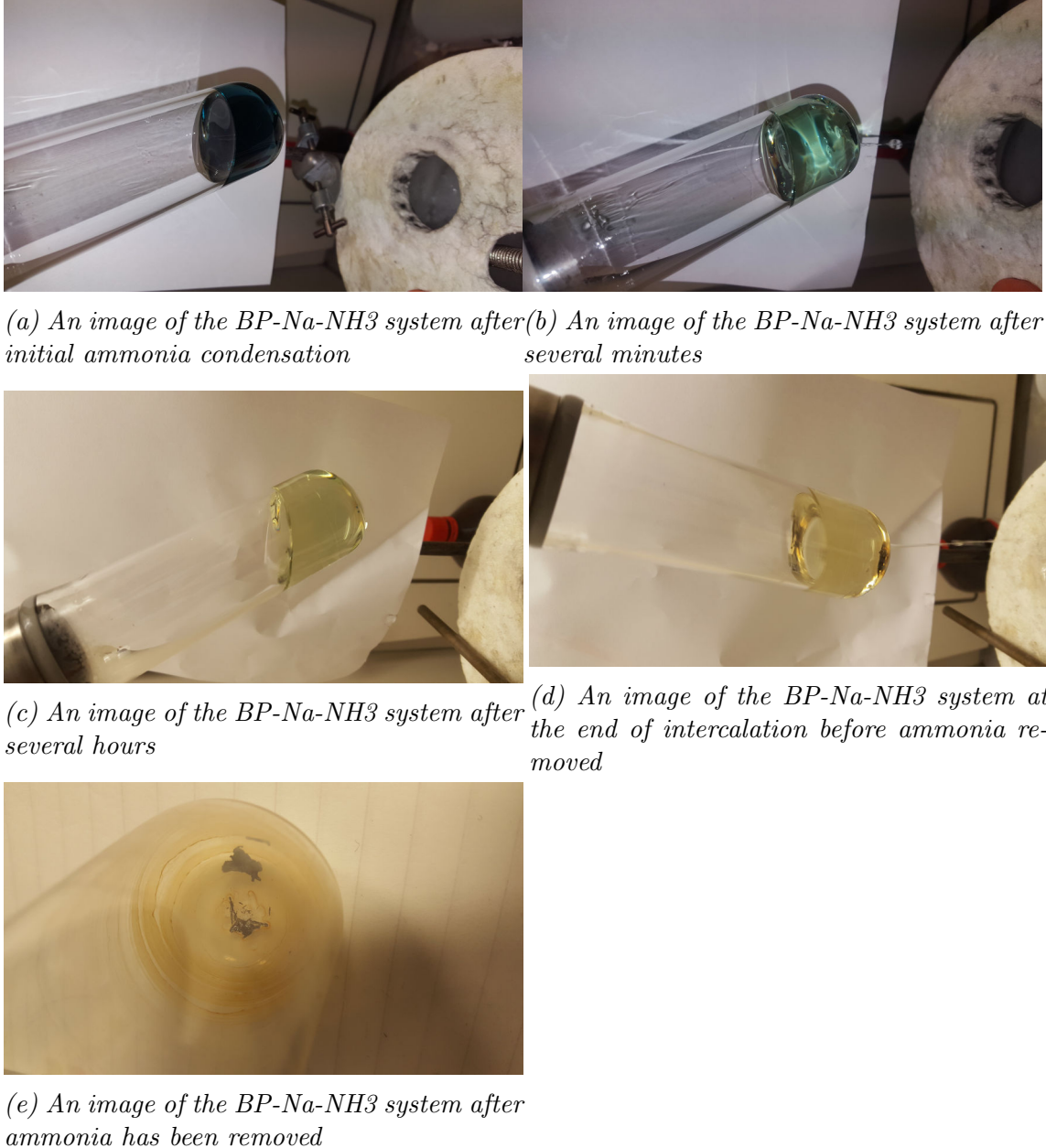


Figure 6.1: Images of the BP-Na-NH<sub>3</sub> system throughout the doping process.

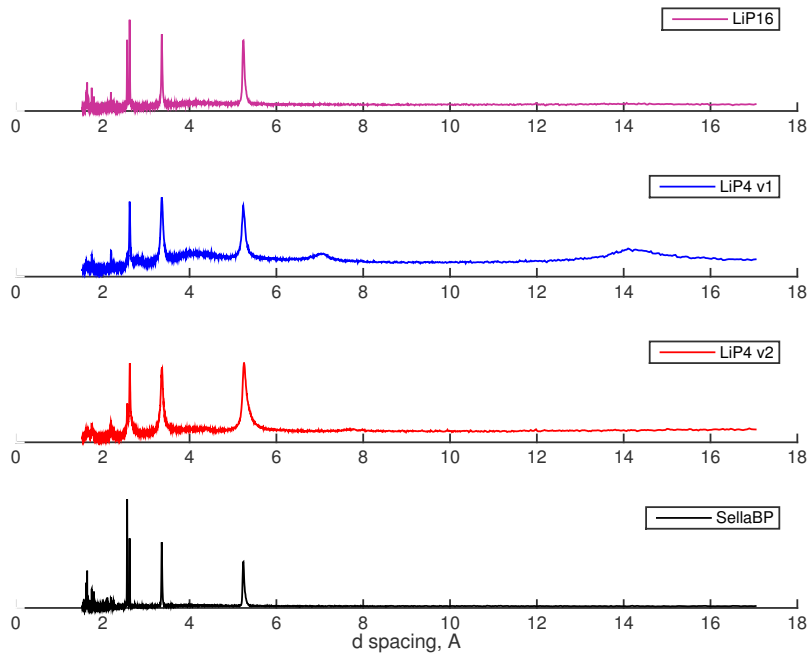


Figure 6.2: Powder XRD of lithium-intercalated black phosphorus

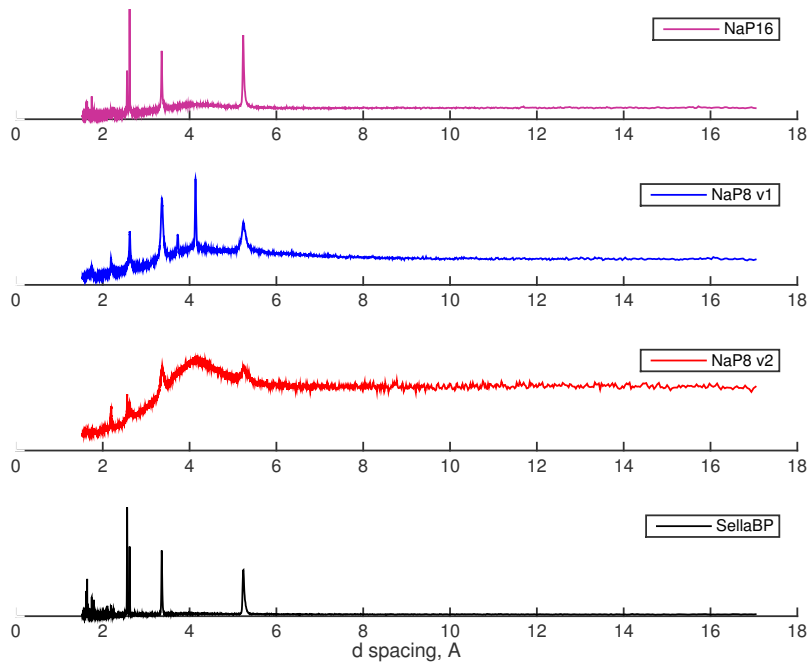
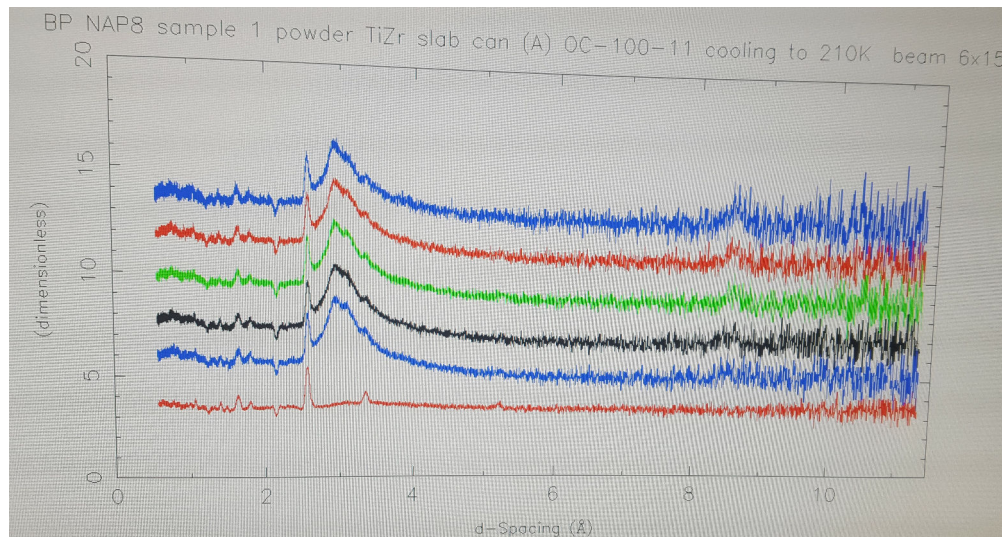


Figure 6.3: Powder XRD of sodium-intercalated black phosphorus



*Figure 6.4: Time resolved diffraction pattern of  $\text{LiP}_8$  ratio during metal-ammonia reduction. (Note issues with data reduction software means better plot is not available)*

#### 6.1.1.3 In-situ neutron diffraction

In-situ neutron diffraction has been undertaken on the POLARIS beamline. Unfortunately a cold spot in the cryostat lead to freezing of the ammonia in the  $\text{Na} - \text{ND}_3$  system, and subsequent melting returned the liquid structure but did not lead to any observable change in BP structure. This is in contrast with previous ex-situ results, suggesting that either different conditions or a contaminant in the ex-situ sample is responsible. It is possible that the use of  $\text{ND}_3$  is responsible for this lack of change, however the freezing of ammonia and use of a metal can could also be responsible.

The in-situ lithium-BP system did show an observable change, with a new broad peak growing at large d-spacing. Due to failure of a module on the POLARIS beamline the experiment was cut short before this change stopped, and so diffraction of the sample in the early stages is all that is available, and ex-situ data will be taken at UCL to reveal the final change in structure (assuming it stopped changing). This sample will be once ammonia has been removed, and so further structural changes cannot be assigned to the final state of the intercalation only. Figure 6.4 shows a snapshot of the observed changes, full analysis is yet to be undertaken and the growth of a high-d feature is the only significance which can be drawn at this time.

#### 6.1.1.4 Xray photoelectron spectroscopy

Initial XPS data has been recorded for several samples, and has revealed interesting data about the surface composition of BP post-reduction, data is shown in figure 6.5. The P 2p peaks which were fitted reveal the presence of phosphorus oxides on the surface, probably due to exposure to air during sample preparation. Additionally, a peak at lower binding energy is seen on the crystals, which is currently not assigned, however may be due to metal phosphides. This peak is also seen on the black phosphorus as produced, and so here it may be tin phosphide.

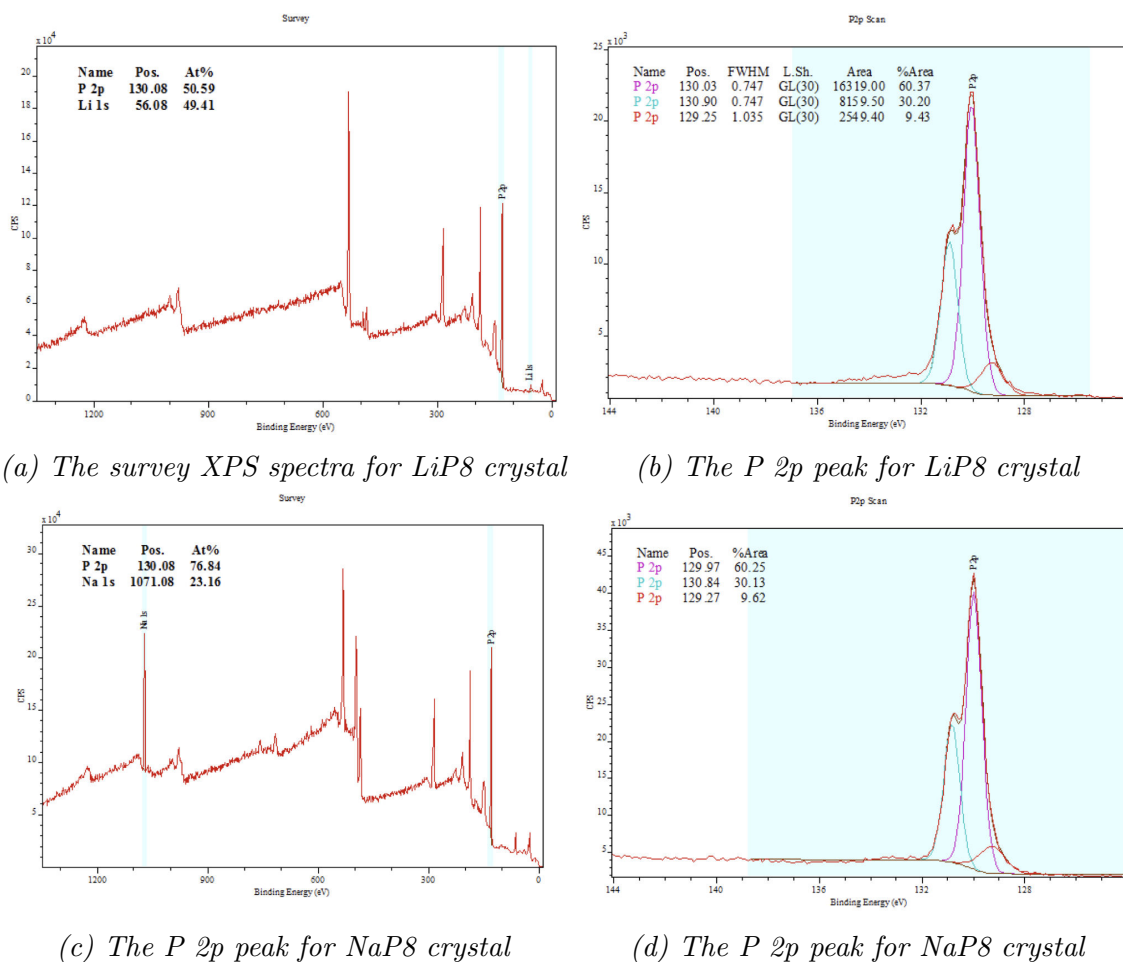


Figure 6.5: XPS data for LiP8 and NaP8 crystals

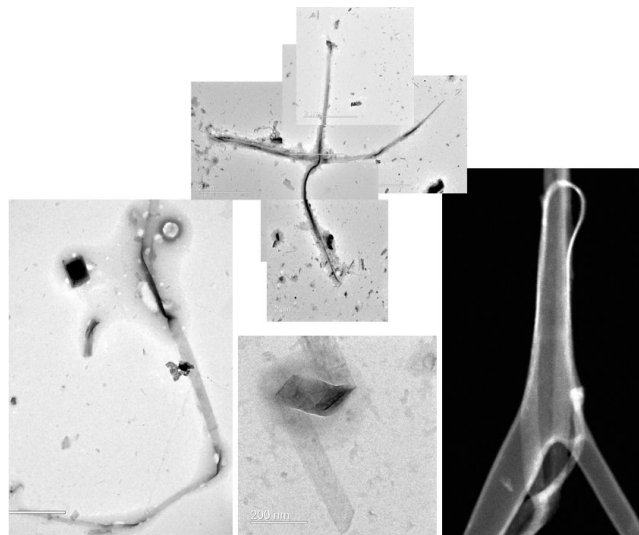


Figure 6.6: An ensemble of TEM images from exfoliated BP following metal-ammonia doping.

The atomic ratios of metal:phosphorus are surprising, however may be misrepresented due to residual phosphides, this will be re-run once phosphides have been removed with ammonia dissolution. If these atomic ratios are accurate, then it suggests that the intercalation process is indeed so slow that there is an accumulation of metal in the surface layers, which may explain the production of phosphides. This may be countered in future by using a powder instead of large crystals, in order to better distribute the metal. It should be noted that the mechanism of black phosphorus ribbon formation is not yet understood, and these phosphides may play an essential role in their production, so it is not necessarily desirable to eliminate their production.

### 6.1.2 Evidence of exfoliation

The reduced crystal has been agitated in suitable solvents and analysed multiple times, this data is presented here.

#### 6.1.2.1 TEM of exfoliated product

TEM has been performed on a JOEL 200 keV electron microscope at UCL and HR-TEM performed on a Titan at EPFL, Switzerland. This data is shown in figure 6.6, which shows an ensemble of interesting ribbon morphologies. There is a rich range of morphology of ribbon produced in these samples, which all show incredible flexibility and well defined edges.

The crystallographic orientation of the ribbons is confirmed in figure 6.7, where diffraction patterns are observed throughout the ribbon. Indexing of this pattern shows that the orientation of the ribbon is along the [100] (zigzag) direction, which is confirmed in all other diffraction patterns for other ribbons. This suggests that the mechanism for formation of these ribbons is not random, and is potentially controllable. Other literature for the formation of cracks and holes in BP flakes hints at

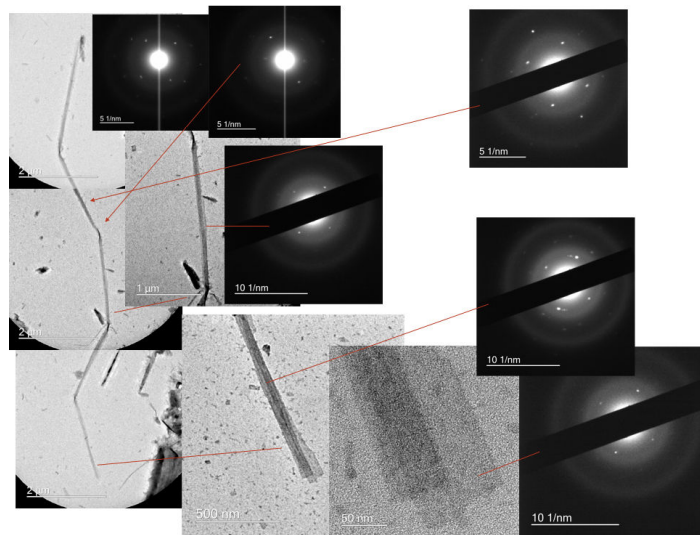


*Figure 6.7: A collection of TEM images and diffraction patterns which show the crystallographic orientation of the BP ribbons is consistent all the way up the ribbon.*

a possible origin for the formation of these ribbons, which is discussed later [20, 93].

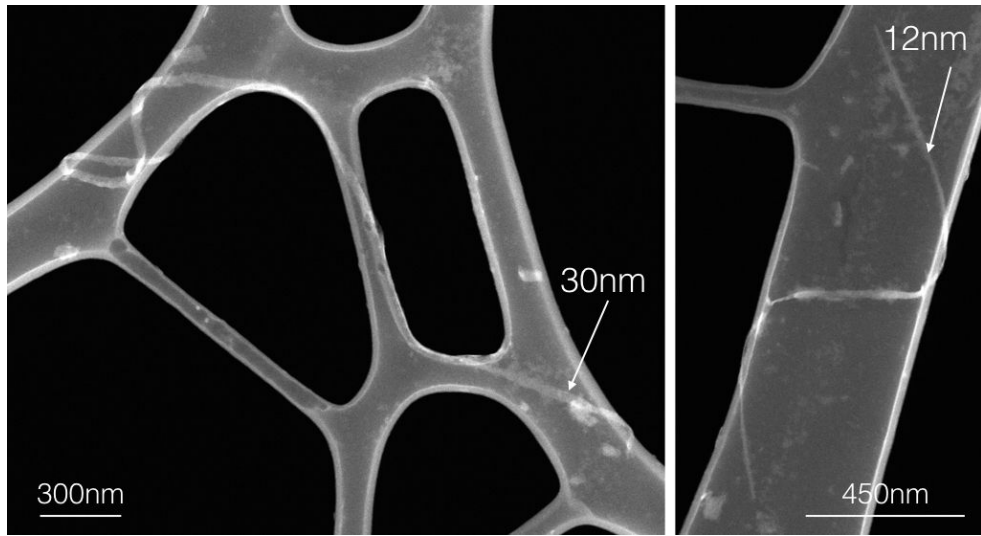
Figure 6.8 shows a very small ribbon, which has a width of the order of 10nm, suggesting that ribbons of this size may be common in these solutions. Due to incomplete removal of solvent it has been difficult to locate ribbons of these size, however any ribbon of less than 8nm is predicted to have quantum confinement effects due to its size, and may be classified as a true nanoribbon. This would be the first time these have been produced in isolation, in a form which can be used for testing and applications.

Figure 6.9a shows a HR-TEM image of the edge of a BP ribbon. Edge roughness is an important characteristic of true nanoribbons, and so statistical analysis of edge roughness will be completed in order to ascertain the typical roughness vs size of ribbon. Rough edges introduce disorder and extra states into the band structure of nanoribbons, and may obscure their interesting properties, for example the extra scattering can drastically reduce the carrier mobilities. Unfortunately, the current data has been taken for high energy electron beams, which likely leads to amorphisation of the edges, additionally incomplete drying means that edges may be obscured by amorphous solvent covering the edges. The edge roughness in figure 6.9a as a % cannot be calculated for this ribbon as it was very wide and the exact width is not known ( $\approx 150\text{nm}$ ). The amorphous edge varies from 0.5nm to 1.9nm over a length of 17nm, the amorphous edge stays in this range but the crystalline edge varies by 1.6nm in one spot, however varies very little otherwise.

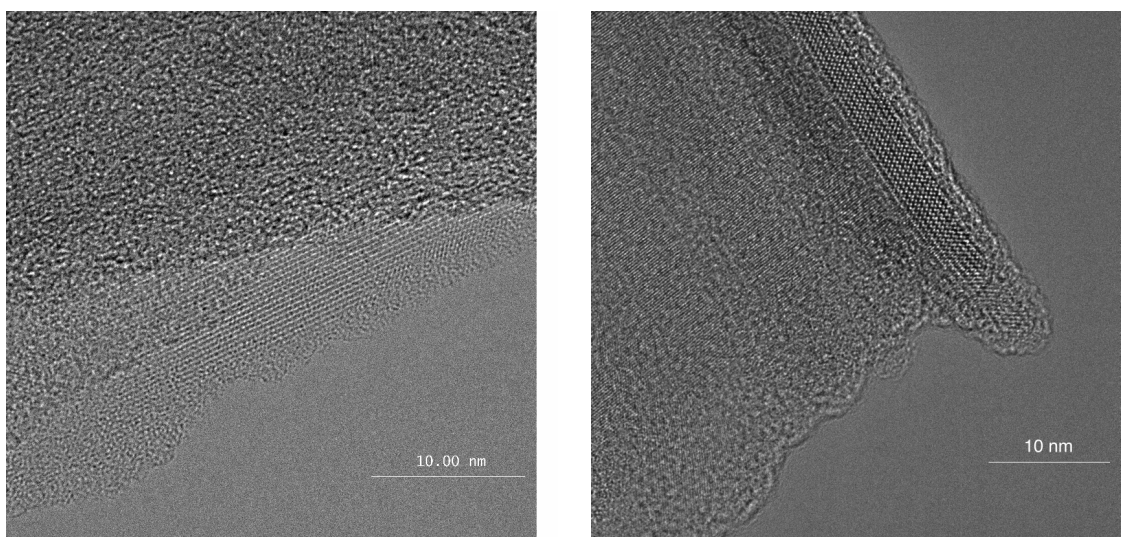
Also, an interesting object found during HRTEM operation looks like a potential nanotube of phosphorene, although it could just be a rolled end, see figure 6.9b.

### 6.1.2.2 AFM of exfoliated product

Peak force tapping AFM was performed at UCL on samples drop cast onto mica substrates. The solvents in these samples were both THF and NMP, however THF



*Figure 6.8: A HR-TEM image showing two ribbons, with one in the range of 10nm which is required to define a nanoribbon.*



*(a) A high resolution TEM image of the edges (b) A rolled phosphorene layer, with an edge of a BP ribbon. which looks like a nanotube.*

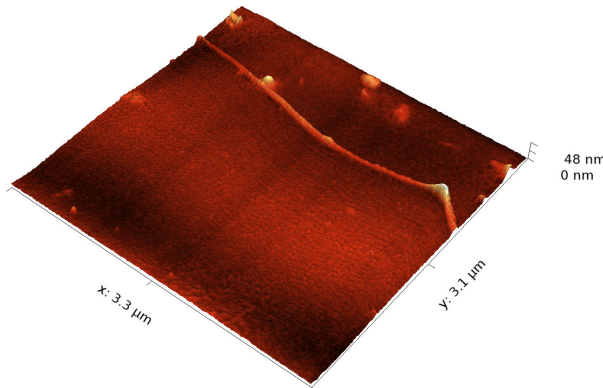


*Figure 6.10: An AFM image showing the dimensions of a BP ribbon on a TEM grid substrate.*

was found to reaggregate (or possibly not exfoliate) the black phosphorus and so was not tested further. NMP samples were often extremely difficult to dry, and AFM often revealed very wet surfaces with no observable objects on the substrate. HS-AFM was thus performed at Bristol in collaboration with Dr. Loren Picco and Dr. Oliver Payton. This HS-AFM is contact mode and allowed the removal of surface liquid to effectively image objects on the substrate. There is also the capability to measure on TEM grid substrates and perform conductive AFM on HOPG which is currently underway. This data confirmed the morphology of objects seen via TEM, and collects essential thickness data which will allow inference of the typical thickness of objects seen via TEM. A typical AFM image is shown in figure 6.10, which shows a thin ribbon which twists on the substrate.

### 6.1.3 Evidence of mechanism

Figures 6.11 and 6.12 show a potential mechanism for the formation of BP ribbons. In figure 6.11, a large flake is seen which has scores along its surface. Ribbons can be seen 'unpeeling' along these scores on the flake, suggesting that the mechanism involves a patterning step. The sample shown was prepared by very gentle stirring. When more rigorous agitation is used these flakes are never seen, suggesting that gentle exfoliation via stirring exfoliates large flakes, which are pre-patterned and are a precursor to ribbon formation. The exact mechanism for the patterning of these sheets is not clear.

Figure 6.12 shows an enlarged area of figure 6.11. The shape of this hole is similar to those seen in the literature by thermal damage to BP sheets or electron beam damage. These processes cause holes of different shapes to grow in different directions, suggesting that these two similar but different methods preferentially target different bonds/atoms in the system. Liu et al. report thermal damage to BP flakes suggests that sublimation is the cause for the growth of holes [93]. Due to opening of a layer around a vacancy, an area below is now a surface which can

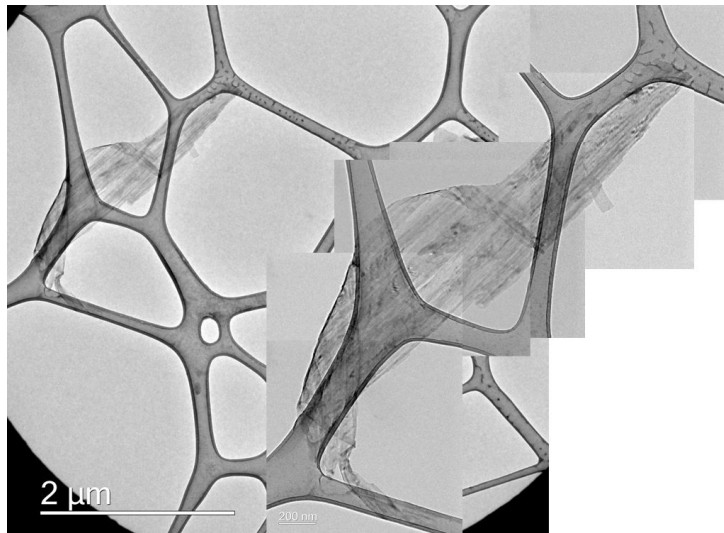


*Figure 6.11: A TEM image of a partially exfoliated BP flake, with ribbons 'unpeeling' along scores on the sheet.*

lead to a new vacancy and growth of a subsequent hole in another layer below.

Masih Das et al. report controllable sculpture of BP nanoribbons suggesting this is the same mechanism as the thermal sublimation result, but makes no note of the different result [20]. This suggests that an electron beam causes the growth of a hole in a flake by a different mechanism, possibly targeting bonds with different electron densities around a vacancy. This is similar to the system being investigated here, where the production of byproduct phosphides is a chemical process which could target bonds based on their electron densities. This suggests that the patterning of holes in black phosphorus may be due to damage of surface sheets by phosphide production, potentially producing these 'scores' seen on the flakes.

Figures 6.13a and 6.13b show another exfoliation of ribbons, here they appear to have been spliced from a larger ribbon, potentially by the same process.

#### 6.1.4 Controls

Multiple groups have performed liquid phase exfoliation on non-reduced/intercalated BP, with no reports of nanoribbon production [13, 94–96]. In addition pristine BP has been bath sonicated in identical solvents and conditions without the reduction step, and has yielded no nanoribbons. One group [61] have report 'nanobelt' objects produced via ultrasonication in similar solvents, however these are microns wide, although do have similar aspect ratios to ribbons discussed in this report. No diffraction of these nanobelts was provided for comparison.

BP in more solvents via stirring only is currently being tested, and will shed light on the process of exfoliation. Large sheets exfoliated this way would be interesting, especially if they have similar patterns, however this is unlikely given the controls already tested.

In future, phosphides will be thoroughly washed and removed before dissolution

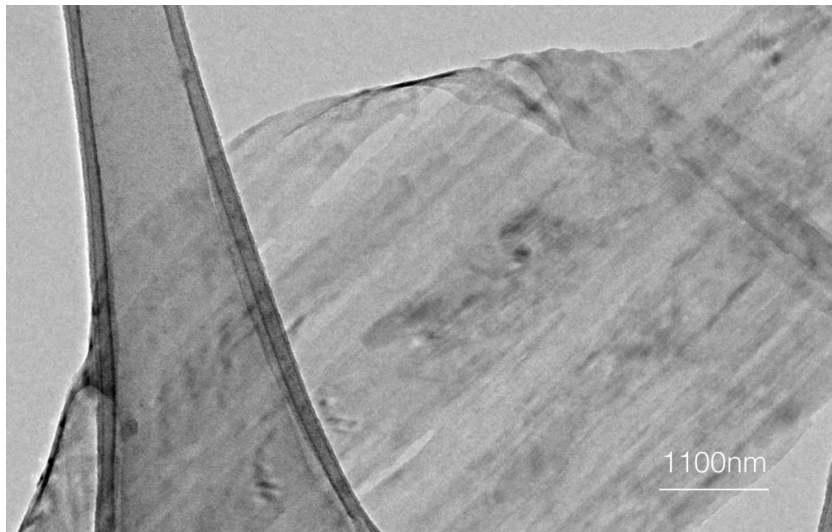
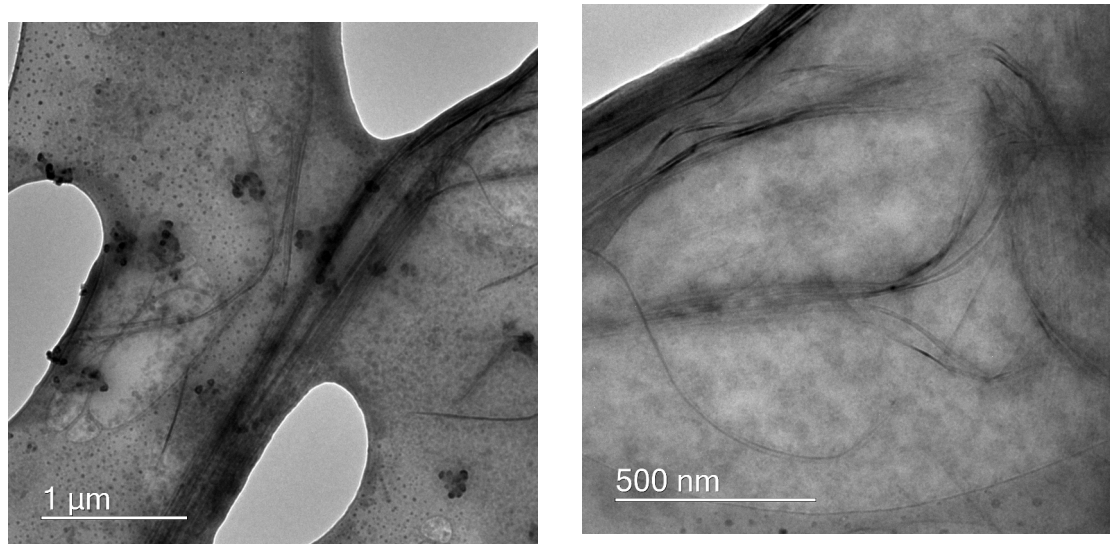


Figure 6.12: A higher magnification TEM image of a partially exfoliated BP flake, with ribbons 'unpeeling' along scores on the sheet.



(a) A TEM image of hair-like structures seen in stirred NaP8-NMP system.

(b) A higher magnification TEM image of hair-like structures seen in stirred NaP8-NMP system.

of BP, if ribbons are still produced then this will suggest that the pre-patterning of sheets occurs during the intercalation step. The use of fine powders, and the aim to reduce the phosphide production may shed light on the role of phosphide production in patterning of BP sheets, and therefore in the ribbon production process.

Multiple new metals will be tested in the future, as will intercalation via other methods such as electrochemically or vapour-phase deposition. The results of these will be compared to current exfoliation products for further insight on the role of metal-ammonia systems in ribbon production.

## 6.2 Planned experiments

In the future, some computational results from a group in Korea will be used (assuming cif files can be obtained) and checked against diffraction patterns and Raman spectra. Multiple metal concentrations, as well as some new attempts with magnesium will be undertaken and analysed. In the past the ex situ results indicate that the intercalant is very heterogeneous, and much of the intercalated compound lies near the surface [59]. For this reason some intercalations will be repeated with finer powders used in order to increase the amount of intercalant. Vapour transport of lithium, sodium and magnesium will also be attempted. Literature suggests that lithium vapour transport only dopes the surfaces, however electrochemical doping has been achieved with sodium so once again fine powders will be used in the hope of intercalating a larger amount of the samples [31]. The XRD patterns will be compared between the ammonia route and the vapour transport route.

Grazing incidence diffraction may also be undertaken in order to characterise the surface vs bulk crystal following intercalation. This will confirm if the intercalant is mostly produced near the surface.

Raman spectra will be recorded for all intercalants, both ammonia and vapour transport. In the past this has proved difficult, with little promising results, however a more comprehensive approach will be taken in order to characterise the samples. Additionally, using the structures for intercalated black phosphorus in the literature, Raman spectra may be computationally predicted - however this has not yet been investigated so may not be possible.

ARPES or UVPS could be used in order to characterise the band structure of the intercalant. Additionally, when dissolved the use of electrophoresis or zeta potentials may also provide evidence for charge transfer to layers.

TGA-mass spectroscopy will be undertaken on the salt in order to reveal the extent of ammonia presence in the salts.

UV-Vis and PL will be used on the solutions to understand the optical properties of the dissolved nanoribbons.

Optical tweezers will be used in order to observe the nanoribbons in solution. SAXS is not suitable for these samples due to the diversity in sizes, and nanoribbons

would need to be approaching 1D in order to see a change in dimensionality on SAS.

SEM will be used on the intercalant in order to see if the 'cracks' which are present on some exfoliated sheets, which ribbons seem to peel off along, are present all over the surface. This may bolster evidence for the proposed mechanism.

The dissolved nanoribbons will be investigated with UV-Vis in order to get a standard for concentration, and use mass filtration in order to give absolute values of these concentrations. Temperature dependence may also be investigated for this.

Further analysis of TEM and AFM will be undertaken in order to produce histograms of sizes and thickness's, and also compare this to sonication vs stirring and also metal type and stoichiometry.

An issue so far has been drying of deposited nanoribbons. This will be further investigated, initially using an optical microscope to identify solvent presence on silicon wafers. The variation of heat and argon flow as well as pumping on substrates will be investigated in order to best dry these. The effect of washing with other solvent will also be investigated. If this works then further HRTEM will be undertaken and mobilities measured on larger ribbons.

Additionally, if possible the crystallite size and orientation of the starting material will be compared to that of the exfoliated flakes. This may be deduced via TEM, XRD and SEM.

## 6.3 Other work

Other work which has been carried out in the previous year and is still ongoing is as follows.

### 6.3.1 Sodium-ion battery anode

An idea for a sodium-ion battery anode is being pursued in collaboration with Dr David Buckley. This idea hopes to use a hybrid of CNT gels and black phosphorus nanoribbons in order to produce a material with extremely high surface area, low density, and large capacity for sodium ion batteries. The BP nanoribbons may provide a fast diffusion pathway for sodium ions into and out of the matrix of the CNT gel. Initial results show intact CNTs and also that CNT gels can be re-doped with metal-ammonia solutions and remain intact.

### 6.3.2 Ogg glasses

Additionally, significant beamtime has been spent attempting to produce Ogg glasses. These are glasses of metal-ammonia solutions which may show interesting properties. So far this has been unsuccessful, but if successful then this will form a major part of the future of this project. Several attempts will be made to produce a glass

by quenching directly from 220k into liquid helium on a SQUID. The SQUID will then confirm/deny any superconductivity, and will also show a change at the glass transition temperature. If successful, then further beamtime will be pursued in order to characterise the structure of the glass, as well as EPR.

Current work is as follows:

- 2-4 October 2015 spent on EMU (muon decay) experiment on  $M - Me - NH_2$  systems
- 4-16 October 2015 spent at SANDALS studying the liquid structure of  $M - NH_3$  glassy systems, and assistance on hydrogen storage materials experiment
- 3-9 November 2015 spent at SANDALS studying the liquid structure of  $M - NH_3$  glassy systems
- 3-8 December 2015 spent at SANDALS studying the liquid structure of  $M - NH_3$  glassy systems
- 3-8 March 2016 spent at SANDALS studying the liquid structure of  $M - NH_3$  glassy systems and ammonia borane hydrogen storage experiment assistance
- 6-9 March 2016 spent studying low-T structure  $M - Me - NH_2$  systems on GEM
- 18-21 March 2016 studying structure and dynamics of low-T  $M - Me - NH_2$  systems on OSIRIS
- 10-20 May 2016 studying spent at SANDALS studying the liquid structure of  $M - NH_3$  glassy systems

A additional week has been spent studying Li-Me-NH<sub>2</sub> magnetic properties using SQUID at the LCN.

### 6.3.3 Additonal beamtime

Additional facilities time has been spent as follows:

- 24-27 October 2016 studying SANS structure of GIC-solvent systems
- 7-12 December 2016 studying black phosphorus intercalation in-situ

# Chapter 7

## Plan and timetable



Figure 7.1: Gantt charts for the remainder of the PhD, ending in Spring 2018

# Black Phosphorus, Phosphorene and Phosphorene Nanoribbons

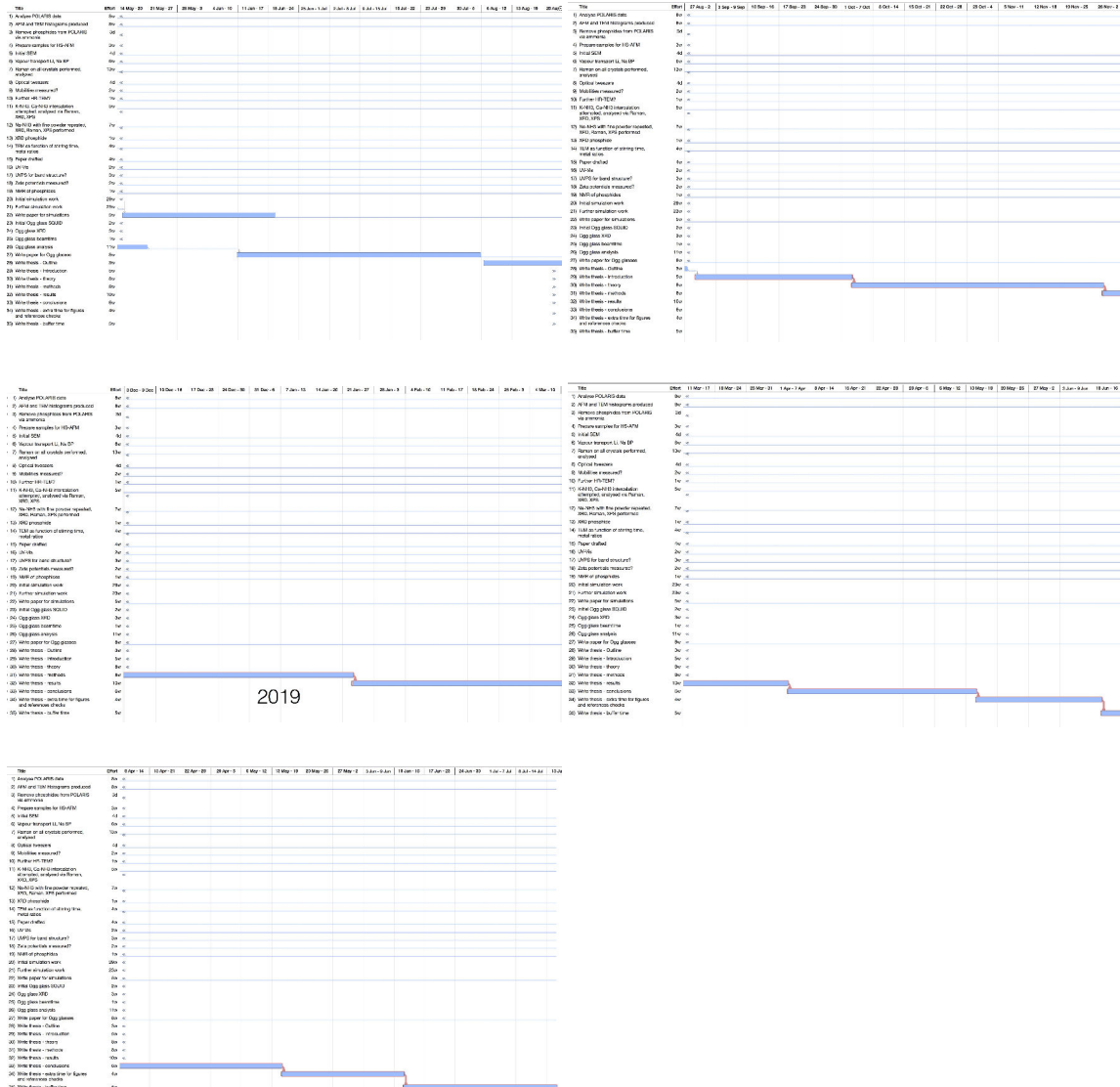


*Figure 7.2: Gantt charts for the remainder of the PhD, ending in Summer 2019*

# Bibliography

- [1] K. S. Novoselov, A. K. Geim, S. V. Morozov, D. Jiang, Y. Zhang, S. V. Dubonos, I.V. Grigorieva, and A. A. Firsov. Electric Field Effect in Atomically Thin Carbon Films. *Science*, 306(5696):666–669, 2004.
- [2] Andres Castellanos-Gomez. Black Phosphorus: Narrow Gap, Wide Applications. *Journal of Physical Chemistry Letters*, 6(21):4280–4291, 2015.
- [3] Bangfu Ding, Wei Chen, Zilong Tang, and Junying Zhang. Tuning Phosphorene Nanoribbon Electronic Structure through Edge Oxidization. *Journal of Physical Chemistry C*, 120(4):2149–2158, 2016.
- [4] Andres Castellanos-Gomez, Leonardo Vicarelli, Elsa Prada, Joshua O. Island, K. L. Narasimha-Acharya, Sofya I. Blanter, Dirk J. Groenendijk, Michele Buscema, Gary a. Steele, J. V. Alvarez, Henny W. Zandbergen, J. J. Palacios, and Herre S. J. van der Zant. Isolation and characterization of few-layer black phosphorus. *2D Materials*, 1(2):025001, 2014.
- [5] John C. Jamieson. Crystal Structures Adopted by. *Science*, 139(6):1291–1292, 1963.
- [6] Zhen Zhu and David Tom??nek. Semiconducting layered blue phosphorus: A computational study. *Physical Review Letters*, 112(17):1–5, 2014.
- [7] Fukuoka Shuhei, Taen Toshihiro, and Osada Toshihito. Electronic structure and the properties of phosphorene systems. *Journal of the Physical Society of Japan*, 84:121004–1 –121004–12, 2015.
- [8] H. Y. Lv, W. J. Lu, D. F. Shao, and Y. P. Sun. Large thermoelectric power factors in black phosphorus and phosphorene. *Cornell University Library*, page 2189, 2014.
- [9] Wilson A. Crichton, Mohamed Mezouar, Giulio Monaco, and Sara Falconi. Phosphorus: New in situ powder data from large-volume apparatus. *Powder Diffraction*, 18(02):155–158, 2003.
- [10] Andres Castellanos-Gomez, Leonardo Vicarelli, Elsa Prada, Joshua O. Island, K. L. Narasimha-Acharya, Sofya I. Blanter, Dirk J. Groenendijk, Michele Buscema, Gary a. Steele, J. V. Alvarez, Henny W. Zandbergen, J. J. Palacios, and Herre S. J. van der Zant. Isolation and characterization of few-layer black phosphorus. *2D Materials*, 1(2):025001, 2014.

- [11] Yuan Huang, Kai He, Stoyan Bliznakov, Eli Sutter, Fanke Meng, Dong Su, and Peter Sutter. Degradation of black phosphorus (BP): The role of oxygen and water. page arXiv 1511.09201, 2015.
- [12] Zhinan Guo, Han Zhang, Shunbin Lu, Zhiteng Wang, Siying Tang, Jundong Shao, Zhengbo Sun, Hanhan Xie, Huaiyu Wang, Xue Feng Yu, and Paul K. Chu. From Black Phosphorus to Phosphorene: Basic Solvent Exfoliation, Evolution of Raman Scattering, and Applications to Ultrafast Photonics. *Advanced Functional Materials*, pages 6996–7002, 2015.
- [13] Adam H. Woomer, Tyler W. Farnsworth, Jun Hu, Rebekah A. Wells, Carrie L. Donley, and Scott C. Warren. Phosphorene: Synthesis, Scale-Up, and Quantitative Optical Spectroscopy. *ACS Nano*, 9(9):8869–8884, 2015.
- [14] V. Wang, Y. C. Liu, Y. Kawazoe, and W. T. Geng. Role of Interlayer Coupling on the Evolution of Band Edges in Few-Layer Phosphorene. *Journal of Physical Chemistry Letters*, 6(24):4876–4883, 2015.
- [15] Xi Ling, Han Wang, Shengxi Huang, Fengnian Xia, and Mildred S. Dresselhaus. The renaissance of black phosphorus. *Proceedings of the National Academy of Sciences*, 112(15):201416581, 2015.
- [16] Joshua O Island, Gary A Steele, Herre S J van der Zant, and Andres Castellanos-Gomez. Environmental instability of few-layer black phosphorus. *2D Materials*, 2(1):011002, 2015.
- [17] Vy Tran and Li Yang. Unusual Scaling Laws of the Band Gap and Optical Absorption of Phosphorene Nanoribbons. *arXiv preprint arXiv:1404.2247*, 2014.
- [18] Qingyun Wu, Lei Shen, Ming Yang, Zhigao Huang, and Yuan Ping Feng. Band Gaps and Giant Stark Effect in Non-Chiral Phosphorene Nanoribbons. pages 1–19, 2014.
- [19] Woosun Jang, Kisung Kang, and Aloysius Soon. Acute Mechano-Electronic Responses in Twisted Phosphorene Nanoribbons. *Nanoscale*, 2016.
- [20] Paul Masih Das, Gopinath Danda, Andrew Cupo, William M. Parkin, Liangbo Liang, Neerav Kharche, Xi Ling, Shengxi Huang, Mildred S. Dresselhaus, Vincent Meunier, and Marija Drndic. Controlled Sculpture of Black Phosphorus Nanoribbons. *ACS Nano*, page acsnano.6b02435, 2016.
- [21] Hongyan Guo, Ning Lu, Jun Dai, Xiaojun Wu, and Xiao Cheng Zeng. Phosphorene Nanoribbons, Phosphorus Nanotubes, and van der Waals Multilayers. *The Journal of Physical Chemistry C*, 118:14051–14059, 2014.
- [22] J Zhang, H J Liu, L Cheng, J Wei, J H Liang, D D Fan, J Shi, X F Tang, and Q. J. Zhang. Phosphorene nanoribbon as a promising candidate for thermo-electric applications. *Scientific reports*, 4:4–10, 2014.
- [23] Alexandre Favron, Etienne Gaufrès, Frédéric Fossard, Anne-Laurence Phaneuf-L'Heureux, Nathalie Y-W Tang, Pierre L Lévesque, Annick Loiseau, Richard

- Leonelli, Sébastien Francoeur, and Richard Martel. Photooxidation and quantum confinement effects in exfoliated black phosphorus. *Nature materials*, 14(8):826–32, 2015.
- [24] Han Liu, Adam T. Neal, Zhen Zhu, David Tomanek, and Peide D. Ye. Phosphorene: A New 2D Material with High Carrier Mobility. *ACS nano*, 4133:4033–4041, 2014.
- [25] Adam T Neal. Phosphorene : An Unexplored 2D Semiconductor with a High Hole Mobility. (4):4033–4041, 2014.
- [26] Jingsi Qiao, Xianghua Kong, Zhi-Xin Hu, Feng Yang, and Wei Ji. High-mobility transport anisotropy and linear dichroism in few-layer black phosphorus. *Nature Communications*, 5:4475, 2014.
- [27] Fengnian Xia, Han Wang, and Yichen Jia. Rediscovering black phosphorus as an anisotropic layered material for optoelectronics and electronics. *Nature communications*, 5:4458, 2014.
- [28] Saptarshi Das, Marcel Demarteau, Andreas Roelofs, Nanoscale Material, High Energy Physics, and United States. Ambipolar Phosphorene Field Effect Transistor. *ACS Nano*, (11):11730–11738, 2014.
- [29] Jingsi Qiao, Xianghua Kong, Zx Hu, Feng Yang, and Wei Ji. Few-layer black phosphorus: emerging direct band gap semiconductor with high carrier mobility. *arXiv preprint arXiv:1401.5045*, 2014.
- [30] Xue-fang Yu, Hiroshi Ushiyama, and Koichi Yamashita. Comparative Study of Sodium and Lithium Intercalation and Diffusion Mechanism in Black Phosphorus from First-principles Simulation. *Chemistry Letters*, 43(12):1940–1942, 2014.
- [31] Jie Sun, Hyun-Wook Lee, Mauro Pasta, Hongtao Yuan, Guangyuan Zheng, Yongming Sun, Yuzhang Li, and Yi Cui. A phosphorene-graphene hybrid material as a high-capacity anode for sodium-ion batteries. *Nature nanotechnology*, 10(11):980–5, 2015.
- [32] Gui-Liang Xu, Zonghai Chen, Gui-Ming Zhong, Yuzi Liu, Yong Yang, Tianyuan Ma, Yang Ren, Xiaobing Zuo, Xue-Hang Wu, Xiaoyi Zhang, and Khalil Amine. Nanostructured Black Phosphorus/Ketjenblack–Multiwalled Carbon Nanotubes Composite as High Performance Anode Material for Sodium-Ion Batteries. *Nano Letters*, page acs.nanolett.6b01777, 2016.
- [33] X Liu, Y W Wen, Z Z Chen, B Shan, and R Chen. A first-principles study of sodium adsorption and diffusion on phosphorene. *Physical Chemistry Chemical Physics*, 17(25):16398–16404, 2015.
- [34] K. P S S Hembram, Hyun Jung, Byung Chul Yeo, Sung Jin Pai, Seungchul Kim, Kwang Ryeol Lee, and Sang Soo Han. Unraveling the Atomistic Sodiation Mechanism of Black Phosphorus for Sodium Ion Batteries by First-Principles Calculations. *Journal of Physical Chemistry C*, 119(27):15041–15046, 2015.

- [35] Mouad Dahbi, Naoaki Yabuuchi, Mika Fukunishi, Kei Kubota, Kuniko Chihara, Kazuyasu Tokiwa, Xue-fang Yu, Hiroshi Ushiyama, Koichi Yamashita, Jin-Young Son, Yi-Tao Cui, Hiroshi Oji, and Shinichi Komaba. Black Phosphorus as a High-Capacity, High-Capability Negative Electrode for Sodium-Ion Batteries: Investigation of the Electrode/Electrolyte Interface. *Chemistry of Materials*, page acs.chemmater.5b03524, 2016.
- [36] Xue Fang Yu, Giacomo Giorgi, Hiroshi Ushiyama, and Koichi Yamashita. First-principles study of fast Na diffusion in Na<sub>3</sub>P. *Chemical Physics Letters*, 612:129–133, 2014.
- [37] Zhaoxin Yu, Jiangxuan Song, Mikhail L. Gordin, Ran Yi, Duihai Tang, and Donghai Wang. Phosphorus-Graphene Nanosheet Hybrids as Lithium-Ion Anode with Exceptional High-Temperature Cycling Stability. *Advanced Science*, 2(1-2):n/a–n/a, 2015.
- [38] Weiwei Xia, Qiubo Zhang, Feng Xu, Hongyu Ma, Jing Chen, Khan Qasim, Binghui Ge, Chongyang Zhu, and Litao Sun. Visualizing the Electrochemical Lithiation/Delithiation Behaviors of Black Phosphorus by in Situ Transmission Electron Microscopy. *Journal of Physical Chemistry C*, 120(11):5861–5868, 2016.
- [39] Long Chen, Guangmin Zhou, Zhibo Liu, Xiaomeng Ma, Jing Chen, Zhiyong Zhang, Xiuliang Ma, Feng Li, Hui Ming Cheng, and Wencai Ren. Scalable Clean Exfoliation of High-Quality Few-Layer Black Phosphorus for a Flexible Lithium Ion Battery. *Advanced Materials*, 28(3):510–517, 2016.
- [40] Qingyun Wu, Lei Shen, Ming Yang, Zhigao Huang, and Yuan Ping Feng. Electronic and Transport Property of Phosphorene Nanoribbon. pages 1–19, 2014.
- [41] Steven P. Koenig, Rostislav A. Doganov, Henrik Schmidt, A. H. Castro Neto, and Barbaros Ozyilmaz. Electric field effect in ultrathin black phosphorus. *Applied Physics Letters*, 104(10):0–4, 2014.
- [42] Han Liu, Yuchen Du, Yexin Deng, and Peide D Ye. Semiconducting black phosphorus: synthesis, transport properties and electronic applications. *Chemical Society Reviews*, 44:2732–2743, 2015.
- [43] Weinan Zhu, Maruthi N. Yogeesh, Shixuan Yang, Sandra H. Aldave, Joon Seok Kim, Sushant Sonde, Li Tao, Nanshu Lu, and Deji Akinwande. Flexible black phosphorus ambipolar transistors, circuits and AM demodulator. *Nano Letters*, 15(3):1883–1890, 2015.
- [44] Jingsi Qiao, Xianghua Kong, Zhi-Xin Hu, Feng Yang, and Wei Ji. High-mobility transport anisotropy and linear dichroism in few-layer black phosphorus. *Nature Communications*, 5:4475, 2014.
- [45] Damien Hanlon, Claudia Backes, Evie Doherty, Clotilde S. Cucinotta, Nina C. Berner, Conor Boland, Kangho Lee, Andrew Harvey, Peter Lynch, Zahra Gholamvand, Saifeng Zhang, Kangpeng Wang, Glenn Moynihan, Anuj Pokle, Quentin M. Ramasse, Niall McEvoy, Werner J. Blau, Jun Wang, Gonzalo Abellán, Frank Hauke, Andreas Hirsch, Stefano Sanvito, David D. O'Regan,

- Georg S. Duesberg, Valeria Nicolosi, and Jonathan N. Coleman. Liquid exfoliation of solvent-stabilized few-layer black phosphorus for applications beyond electronics. *Nature Communications*, 6:8563, 2015.
- [46] S Sugai. RAMAN AND INFRARED REFLECTION SPECTROSCOPY IN BLACK PHOSPHORUS. 53(9):753–755, 1984.
- [47] Ruixiang Fei, Alireza Faghaninia, Ryan Soklaski, Jia-an Yan, Cynthia Lo, and Li Yang. Enhanced Thermoelectric Efficiency via Orthogonal Electrical and Thermal Conductances in Phosphorene. 2014.
- [48] Nannan Mao, Juanxia Wu, Bowen Han, Jingjing Lin, Lianming Tong, and Jin Zhang. Birefringence-Directed Raman Selection Rules in 2D Black Phosphorus Crystals. *Small*, pages 2627–2633, 2016.
- [49] Henrique B. Ribeiro, Marcos A. Pimenta, Christiano J S De Matos, Roberto Luiz Moreira, Aleksandr S. Rodin, Juan D. Zapata, Eunézio A T De Souza, and Antonio H. Castro Neto. Unusual angular dependence of the Raman response in black phosphorus. *ACS Nano*, 9(4):4270–4276, 2015.
- [50] Long Chen, Guangmin Zhou, Zhibo Liu, Xiaomeng Ma, Jing Chen, Zhiyong Zhang, Xiuliang Ma, Feng Li, Hui Ming Cheng, and Wencai Ren. Scalable Clean Exfoliation of High-Quality Few-Layer Black Phosphorus for a Flexible Lithium Ion Battery. *Advanced Materials*, 28(3):510–517, 2016.
- [51] Shuang Zhang, Jiong Yang, Renjing Xu, Fan Wang, Weifeng Li, Muhammad Ghufran, Yong Wei Zhang, Zongfu Yu, Gang Zhang, Qinghua Qin, and Yuerui Lu. Extraordinary photoluminescence and strong temperature/angle-dependent raman responses in few-layer phosphorene. *ACS Nano*, 8(9):9590–9596, 2014.
- [52] M. T. Edmonds, A. Tadich, A. Carvalho, A. Ziletti, K. M. O'Donnell, S. P. Koenig, D. F. Coker, B. ??zyilmaz, A. H Castro Neto, and M. S. Fuhrer. Creating a stable oxide at the surface of black phosphorus. *ACS Applied Materials and Interfaces*, 7(27):14557–14562, 2015.
- [53] A. Ziletti, A. Carvalho, D. K. Campbell, D. F. Coker, and A. H. Castro Neto. Oxygen defects in phosphorene. *Physical Review Letters*, 114(4):3–7, 2015.
- [54] Alexandre Favron, Etienne Gaufrès, Frédéric Fossard, Anne-Laurence Phaneuf-L'Heureux, Nathalie Y-W Tang, Pierre L Lévesque, Annick Loiseau, Richard Leonelli, Sébastien Francoeur, and Richard Martel. Photooxidation and quantum confinement effects in exfoliated black phosphorus. suppl. *Nature materials*, 14(8):826–832, 2015.
- [55] Gaoxue Wang, William J. Slough, Ravindra Pandey, and Shashi P. Karna. Degradation of Phosphorene in Air: Understanding at Atomic Level. *2D Materials*, 3(2):1–7, 2015.
- [56] Marianne Kopf, Nadine Eckstein, Daniela Pfister, Carolin Grotz, Ilona Kr??ger, Magnus Greiwe, Thomas Hansen, Holger Kohlmann, and Tom Nilges. Access and in situ growth of phosphorene-precursor black phosphorus. *Journal of Crystal Growth*, 405:6–10, 2014.

- [57] Xuesong Li, Bingchen Deng, Xiaomu Wang, Sizhe Chen, Michelle Vaisman, Shun-ichiro Karato, Grace Pan, Minjoo Larry Lee, Judy Cha, Han Wang, and Fengnian Xia. Synthesis of thin-film black phosphorus on a flexible substrate. *2D Materials*, 2(3):031002, 2015.
- [58] Jiajie Pei, Xin Gai, Jiong Yang, Xibin Wang, Zongfu Yu, Duk-Yong Choi, Barry Luther-Davies, and Yuerui Lu. Producing air-stable monolayers of phosphorene and their defect engineering. *Nature communications*, 7:10450, 2016.
- [59] A Sanna, A V Fedorov, N I Verbitskiy, J Fink, C Krellner, L Petaccia, A Chikina, D Yu Usachov, A Grüneis, and G Profeta. First-principles and angle-resolved photoemission study of lithium doped metallic black phosphorous. *2D Materials*, 3(2):025031, 2016.
- [60] Mamoru Baba, Fukunori Izumida, Akira Morita, Yoji Koike, and Tetsuro Fukase. Electrical properties of black phosphorus single crystals prepared by the bismuth-flux method. *Japanese Journal of Applied Physics*, 30(8):1753–1758, 1991.
- [61] Jie Sun, Hyun-Wook Lee, Mauro Pasta, Hongtao Yuan, Guangyuan Zheng, Yongming Sun, Yuzhang Li, and Yi Cui. A phosphorene-graphene hybrid material as a high-capacity anode for sodium-ion batteries. suppl. *Nature nanotechnology*, 10(11):980–5, 2015.
- [62] Sangwook Lee, Fan Yang, Joonki Suh, Sijie Yang, Yeonbae Lee, Guo Li, Hwan Sung Choe, Aslihan Suslu, Yabin Chen, Changhyun Ko, Joonsuk Park, Kai Liu, Jingbo Li, Kedar Hippalgaonkar, Jeffrey J. Urban, Sefaattin Tongay, and Junqiao Wu. Anisotropic in-plane thermal conductivity of black phosphorus nanoribbons at temperatures higher than 100 K. *Nature Communications*, 6:8573, 2015.
- [63] Xiaohua Wu, Xiaoli Zhang, Xianlong Wang, Zhi Zeng, Xiaohua Wu, Xiaoli Zhang, Xianlong Wang, and Zhi Zeng. Spin density waves predicted in zigzag puckered phosphorene , arsenene and antimonene nanoribbons Spin density waves predicted in zigzag puckered phosphorene , arsenene and antimonene nanoribbons. 045318(May):0–8, 2016.
- [64] Mirko Poljak and Tomislav Suligoj. Immunity of electronic and transport properties of phosphorene nanoribbons to edge defects. *Nano Research*, 9(6):1723–1734, 2016.
- [65] Yu-Rong Yang, Zhao-Qian Zhang, Lei Gu, and Hua-Hua Fu. Spin-dependent Seebeck effect in zigzag black phosphorene nanoribbons. *RSC Adv.*, 6(50):44019–44023, 2016.
- [66] Guang Yang, Shenglong Xu, Wei Zhang, and Congjun Wu. Room temperature magnetism on the zigzag edges of phosphorene nanoribbons. pages 1–5.
- [67] R Ma, H Geng, W Y Deng, M N Chen, L Sheng, and D Y Xing. Effect of the edge states on the conductance and thermopower in Zigzag Phosphorene Nanoribbons. pages 1–6, 2016.

- [68] Xihong Peng and Qun Wei. Chemical scissors cut phosphorene nanostructures and their novel electronic properties. *Arxiv*, page 14, 2014.
- [69] Da Wang, Gen Cai Guo, Xiao Lin Wei, Li Min Liu, and Shi Jin Zhao. Phosphorene ribbons as anode materials with superhigh rate and large capacity for Li-ion batteries. *Journal of Power Sources*, 302:215–222, 2016.
- [70] Ville Vierimaa, Arkady Krasheninnikov, and Hannu-Pekka Komsa. Phosphorene under electron beam: from monolayer to one-dimensional chains. *Nanoscale*, pages 25–28, 2016.
- [71] Zahra Nourbakhsh and Reza Asgari. Excitons and optical spectra of phosphorene nanoribbons. pages 1–9, 2016.
- [72] Vasili Perebeinos, J. Tersoff, and Phaedon Avouris. Radiative lifetime of excitons in carbon nanotubes. *Nano Letters*, 5(12):2495–2499, 2005.
- [73] Maurizia Palummo, Federico Iori, Rodolfo Del Sole, and Stefano Ossicini. Giant excitonic exchange splitting in Si nanowires: First-principles calculations. *Physical Review B - Condensed Matter and Materials Physics*, 81(12):1–4, 2010.
- [74] Shouting Huang, Yufeng Liang, and Li Yang. Exciton spectra in two-dimensional graphene derivatives. *Physical Review B - Condensed Matter and Materials Physics*, 88(7):1–6, 2013.
- [75] J. C. Thompson. *Electrons in Liquid Ammonia*. Oxford University Press, Oxford, 1976.
- [76] Eva Zurek, Peter P Edwards, and Roald Hoffmann. A Molecular Perspective on Lithium – Ammonia Solutions List of Figures. *Angewandte Chemie (International ed. in English)*, 48(Suppl):8198, 2009.
- [77] S A Solin. Graphite Intercalation Compounds. I(September), 1990.
- [78] S.a. Solin and H. Zabel. The physics of ternary graphite intercalation compounds. *Advances in Physics*, 37(March 2015):87–254, 1988.
- [79] Lucy Campbell. No Title, 2013.
- [80] C.a. Silvera Batista, R.G. Larson, and N.a. Kotov. Nonadditivity of nanoparticle interactions. *Science*, 350(6257):1242477\_1–1242477\_10, 2015.
- [81] Mirijam Zobel, Reinhard B Neder, and Simon a J Kimber. Universal solvent restructuring induced by colloidal nanoparticles. *Science*, 347(6219):292–294, 2015.
- [82] Mustafa Lotya, Yenny Hernandez, Paul J. King, Ronan J. Smith, Valeria Nicolosi, Lisa S. Karlsson, Fiona M. Blighe, Sukanta De, Wang Zhiming, I. T. McGovern, Georg S. Duesberg, and Jonathan N. Coleman. Liquid phase production of graphene by exfoliation of graphite in surfactant/water solutions. *Journal of the American Chemical Society*, 131(10):3611–3620, 2009.

- [83] Keith R. Paton, Eswaraiah Varrla, Claudia Backes, Ronan J. Smith, Umar Khan, Arlene O'Neill, Conor Boland, Mustafa Lotya, Oana M. Istrate, Paul King, Tom Higgins, Sebastian Barwick, Peter May, Paweł Puczkarski, Iftikhar Ahmed, Matthias Moebius, Henrik Pettersson, Edmund Long, João Coelho, Sean E. O'Brien, Eva K. McGuire, Beatriz Mendoza Sanchez, Georg S. Duesberg, Niall McEvoy, Timothy J. Pennycook, Clive Downing, Alison Crossley, Valeria Nicolosi, and Jonathan N. Coleman. Scalable production of large quantities of defect-free few-layer graphene by shear exfoliation in liquids. *Nature Materials*, 13(6):624–630, 2014.
- [84] Jonathan N Coleman, Mustafa Lotya, Arlene O'Neill, Shane D Bergin, Paul J King, Umar Khan, Karen Young, Alexandre Gaucher, Sukanta De, Ronan J Smith, Igor V Shvets, Sunil K Arora, George Stanton, Hye-Young Kim, Kangho Lee, Gyu Tae Kim, Georg S Duesberg, Toby Hallam, John J Boland, Jing Jing Wang, John F Donegan, Jaime C Grunlan, Gregory Moriarty, Aleksey Shmelev, Rebecca J Nicholls, James M Perkins, Eleanor M Grieveson, Koenraad Theuwissen, David W McComb, Peter D Nellist, and Valeria Nicolosi. Two-dimensional nanosheets produced by liquid exfoliation of layered materials. *Science (New York, N.Y.)*, 331(6017):568–571, 2011.
- [85] Sasha Stankovich, Dmitriy A. Dikin, Richard D. Piner, Kevin A. Kohlhaas, Alfred Kleinhammes, Yuanyuan Jia, Yue Wu, Son Bin T Nguyen, and Rodney S. Ruoff. Synthesis of graphene-based nanosheets via chemical reduction of exfoliated graphite oxide. *Carbon*, 45(7):1558–1565, 2007.
- [86] Emily M Milner, Neal T Skipper, Christopher A Howard, Milo S P Sha, David J Buckley, K Adam Rahnejat, Patrick L Cullen, Richard K Heenan, Peter Lindner, and Ralf Schweins. Structure and Morphology of Charged Graphene Platelets in Solution by Small-Angle Neutron Scattering. *Journal of the American Chemical Society*, 134(20):8302–8305, 2012.
- [87] Patrick L. Cullen, Kathleen M. Cox, Mohammed K. Bin Subhan, Loren Picco, Oliver D. Payton, David J. Buckley, Thomas S. Miller, Stephen A. Hodge, Neal T. Skipper, Vasiliki Tileli, and Christopher A. Howard. Ionic solutions of two-dimensional materials. *Nature Chemistry*, (November), 2016.
- [88] Michael A. Boles, Daishun Ling, Taeghwan Hyeon, and Dmitri V. Talapin. The surface science of nanocrystals. *Nature Materials*, 15(2):141–153, 2016.
- [89] Jan C. Hummelen, Brian W Knight, and Fred Wudl. Preparation and Characterization of Fulleroid and Methanofullerene Derivatives. *J. Org. Chem.*, 60(21):532–538, 1995.
- [90] Manfred Scheer, Gabor Balazs, and Andreas Seitz. P 4 Activation by Main Group Elements and Compounds. *Chemical Reviews*, 110:4236–4256, 2010.
- [91] E Charles and B Y E Charles. The Alkali Metal Phosphides . I . Reaction of Alkali Metals and White Phosphorus in Liquid Ammonia<sub>1s2</sub>. 323(8):2038–2040, 1937.

- [92] Renyan Zhang, I. Ling Tsai, James Chapman, Ekaterina Khestanova, John Waters, and Irina V. Grigorieva. Superconductivity in Potassium-Doped Metallic Polymorphs of MoS<sub>2</sub>. *Nano Letters*, 16(1):629–636, 2016.
- [93] Xiaolong Liu, Joshua D. Wood, Kan Sheng Chen, Eunkyoung Cho, and Mark C. Hersam. In situ thermal decomposition of exfoliated two-dimensional black phosphorus. *Journal of Physical Chemistry Letters*, 6(5):773–778, 2015.
- [94] Damien Hanlon, Claudia Backes, Evie Doherty, Clotilde S. Cucinotta, Nina C. Berner, Conor Boland, Kangho Lee, Andrew Harvey, Peter Lynch, Zahra Gholamvand, Saifeng Zhang, Kangpeng Wang, Glenn Moynihan, Anuj Pokle, Quentin M. Ramasse, Niall McEvoy, Werner J. Blau, Jun Wang, Gonzalo Abellán, Frank Hauke, Andreas Hirsch, Stefano Sanvito, David D. O'Regan, Georg S. Duesberg, Valeria Nicolosi, and Jonathan N. Coleman. Liquid exfoliation of solvent-stabilized few-layer black phosphorus for applications beyond electronics. *Nature Communications*, 6:8563, 2015.
- [95] Joohoon Kang, Joshua D. Wood, Spencer A. Wells, Jae Hyeok Lee, Xiaolong Liu, Kan Sheng Chen, and Mark C. Hersam. Solvent exfoliation of electronic-grade, two-dimensional black phosphorus. *ACS Nano*, 9(4):3596–3604, 2015.
- [96] Jing-yin Xu, Lin-feng Gao, Chen-xia Hu, Zhi-yuan Zhu, Min Zhao, Qiang Wang, and Hao-li Zhang. Preparation of large size, few-layer black phosphorus nanosheets via phytic acid-assisted liquid exfoliation. *Chemical Communications*, 52:8107–8110, 2016.